Cancer Imaging

REVIEW

Open Access

Current trends in the characterization and monitoring of vascular response to cancer therapy

Binita Shrestha[1*], Noah B Stern[1], Annie Zhou[1], Andrew Dunn[1] and Tyrone Porter[1]

Abstract

Tumor vascular physiology is an important determinant of disease progression as well as the therapeutic outcome of cancer treatment. Angiogenesis or the lack of it provides crucial information about the tumor's blood supply and therefore can be used as an index for cancer growth and progression. While standalone anti-angiogenic therapy demonstrated limited therapeutic benefits, its combination with chemotherapeutic agents improved the overall survival of cancer patients. This could be attributed to the effect of vascular normalization, a dynamic process that temporarily reverts abnormal vasculature to the normal phenotype maximizing the delivery and intratumor distribution of chemotherapeutic agents. Longitudinal monitoring of vascular changes following antiangiogenic therapy can indicate an optimal window for drug administration and estimate the potential outcome of treatment. This review primarily focuses on the status of various imaging modalities used for the longitudinal characterization of vascular changes before and after anti-angiogenic therapies and their clinical prospects.

Background

Angiogenesis, the formation of new blood vessels, is a tightly regulated physiological process essential for tissue development and repair. It is vital for the continued growth of solid tumors as blood vessels serve as conduits for the delivery of oxygen and nutrients to support cell proliferation and the removal of waste to avoid cell toxicity. Scientists hypothesized that shutting down and possibly destroying tumor vasculature with antiangiogenic drugs would lead to cancer cell death and tumor regression. While initial studies of anti-angiogenic therapy against solid tumors produced encouraging results [1], the treatment strategy did not prove to be significantly more effective than the standard of care in clinical trials [2]. Interestingly, studies have reported that the efficacy of chemotherapeutic drugs was improved when combined with an antiangiogenic agent [3–5]. For example, the anti-VEGF antibody bevacizumab increased the survival of colorectal cancer patients by 5 months when combined with chemotherapy [6]. Whereas tumor vasculature is leaky and disorganized, scientists have speculated that anti-angiogenic agents allow blood vessels to seal properly and distribute more uniformly throughout tumors. In theory, the "normalized" vasculature would enhance the delivery of chemotherapy to a solid tumor, leading to a better therapeutic outcome. In addition, normalized vessels reprogram the tumor microenvironment (TME) by reducing tissue hypoxia and inducing an immune-supportive state [7]. Successful execution of this combinatorial/multifactorial treatment strategy would require optimizing the timing between administering antiangiogenic and cytotoxic agents, which is not trivial.

Vascular normalization is a dynamic process. Research and investigations have provided critical insights into understanding this process and an optimal time frame for

*Correspondence:
Binita Shrestha
Binita.shrestha@utexas.edu
[1] Department of Biomedical Engineering, The University of Texas at Austin, Austin, TX 78712, USA

anticancer drug administration to maximize therapeutic efficacy. The optimal period, also known as the "normalization window", refers to a transient period where the vessels are morphologically and functionally comparable to fully developed blood vessels (Fig. 1). Studies have shown that judicious application of antiangiogenic agents prunes immature vessels, and the remaining vasculature is less fenestrated and more uniformly distributed throughout the tumor. Ideally, cytotoxic drugs would be administered during the "normalization window" to maximize delivery and intratumor distribution. The onset and length of the normalization window, however, are time and dose-dependent and vary among different cancer types [8]. Thus, the tumor vascular response to antiangiogenic therapy must be monitored longitudinally to determine when the vessels have been normalized, at which point anticancer agents can be administered.

Various strategies such as histological staining, biomarker profiling, and imaging have been used to monitor vascular changes and evaluate the efficacy of anti-angiogenic treatment. Although histological staining is the gold standard for the detection of vascular normalization, it is not a viable option for longitudinal assessment of changes to tumor vasculature. Tissue-based or circulating molecular and cellular biomarkers can also be examined, but these require invasive procedures and provide information at the systemic level rather than localized to the tumor [9]. In the quest to longitudinally monitor vascular response to direct or indirect anti-angiogenic therapy, various imaging modalities have been explored, including intravital imaging [10, 11], MRI [12–14], CT [15, 16], PET [17, 18], ultrasound [19], and photoacoustic imaging [20–22]. Each of these imaging modalities has strength and limitation when it comes to vascular imaging (Table 1). Image-derived parameters such as tumor oxygen saturation, vessel morphology, vascular density, and blood perfusion have been used as metrics for monitoring vascular remodeling, shutdown, and normalization [23]. In this review, we will discuss and compare different imaging modalities that are used for characterizing vasculature before and after anti-angiogenic therapies and their clinical prospects followed by various standard validation methods that are currently used.

Magnetic resonance imaging

MRI is one of the most frequently used imaging modalities for cancer studies and has become an important tool for researchers interested in observing the vasculature [67–69]. For vascular normalization investigations, MRI is often applied clinically for long-term studies interested in determining normalization windows, analyzing the potential of co-administered chemotherapeutics, and the overall response of the tumor microenvironment. There are a variety of MRI-based techniques that rely

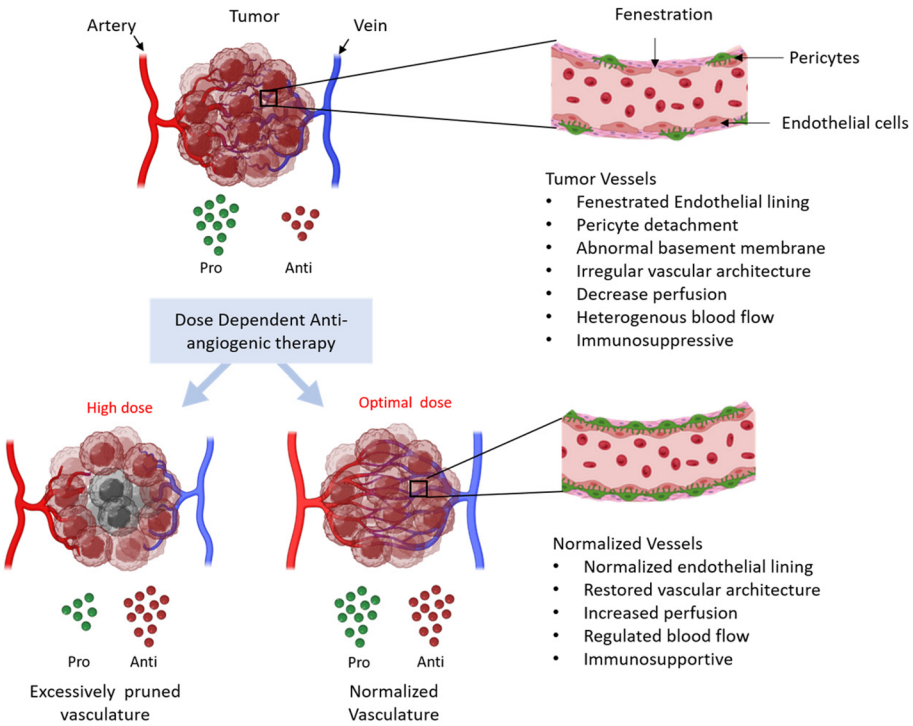

Fig. 1 Schematic illustration of vascular normalization following anti-angiogenic therapy

Table 1 Imaging Modalities Summary. Includes spatial and temporal resolutions, maximum effective depth, advantages, and disadvantages for the major modalities discussed. Components of the chart are focused on vasculature imaging purposes and are slightly different than the optimal values often reported for more general imaging procedures. For example, certain MRI and CT methodologies can give less than 100µm resolutions. Also, not included are potential super resolution methodologies which may dramatically improve or alter certain methodologies. As discussed, super resolution may play an important role in the of future ultrasound and photoacoustic vascular imaging

Modality	Subtype	Spatial Resolution	Temporal Resolution	Depth	Advantages	Disadvantages	References
MRI	DCE-MRI	~1-3mm^3 voxel ~1 - 1.5mm axial	Minutes-Hours	Limitless	No ionizing radiation, limitless penetration depth, high signal to noise ratio, clinically accessible and relevant, whole-body imaging	Easily influenced by motion artifacts, very long scan times, can be high cost and various difficulties associated with siting and scheduling	[24–26]
	DSC-MRI	~2-10mm^3 voxel ~1 - 2.5mm axial	Minutes-Hours	Limitless			[27–29]
CT	Perfusion-CT	5mm axial	Minutes	Limitless	Faster than MRI imaging, limitless penetration depth, whole-body imaging, widespread clinical and pre-clinical availability	High ionizing radiation, high demand on clinical systems already in use, high-end scanners which improve resolution can be expensive	[30–33]
	DECT	0.5 - 2.5mm axial	Minutes	Limitless			[34–38]
PET		~1-10mm axial	Minutes	Limitless	Limitless penetration depth, whole-body imaging, can directly investigate biochemical processes in the region of interest	Low resolution, high ionizing radiation, high costs	[38–42]
OPTICAL	OCTA	1-15µm	Seconds-Minutes	<1cm	Certain techniques can give excellent resolution, real-time imaging, low cost, wide variety in imaging techniques and fluorophores of interest	High susceptibility to artifacts, scattering, and autofluorescence in imaging region, high resolution techniques either have extremely limited imaging depths or require an invasive procedure, limited clinical application	[43–45]
	OT	~1cm	Seconds-Minutes	10cm			[46–48]
	CLE	~1-3µm	Seconds-Minutes	60-250µm			[49–53]
ULTRASOUND	CE-US	0.1-0.5mm	Seconds-Minutes	~12-15cm	Low cost, clinically available and prevalent, non-invasive, no ionizing radiation, real time imaging, high spatial and temporal resolution	Non-intuitive imaging that is operator dependent and difficult to interpret, limited field of view, high susceptibility to tissue artifacts and potentially limited depth	[54–57]
	DCE-US	0.2-2mm	Seconds-Minutes	~12-15cm			[57–59]
PHOTOACOUSTIC	PAM	OR-PAM: 1-2µm AR-PAM: 15-40µm	Seconds-Minutes	OR-PAM: 1mm AR-PAM: 3mm	Multispectral imaging allows for differentiation of endogenous and exogenous agents, no ionizing radiation, real time imaging, high spatial and temporal resolution	Limited availability, not yet clinically prevalent, large tradeoff between resolution and imaging depth, operator dependent	[60–62]
	PAT	100µm (depth dependent)	Seconds-Minutes	4-8cm			[63–66]

on contrast agents and different protocols that allow for structural, functional, and molecular imaging.

Dynamic contrast enhanced MRI

Dynamic Contrast-Enhanced MRI (DCE-MRI) has been used to monitor vascular changes during tumor growth or regression or in response to anti-angiogenic therapy [70]. DCE-MRI relies on the use of gadolinium-based (Gd) paramagnetic contrast agents such as Gadobutrol and Gadodiamide that are administered systemically. For microvessels and broad neovascular imaging more specific agents like Gd-DTPA and Gd-EOB-DTPA show promise [71, 72]. DCE-MRI typically focuses on T1-weighted images as Gd is known to shorten the T1 and T2 relaxation times [73]. Images are acquired before, during, and after the contrast material has flowed into and through the tissue of interest. The acquired MR signal is used to generate a time-intensity curve (TIC) that corresponds to the arrival of the contrast agent represented in enhancement values. Pharmacokinetic models, such as the Tofts model [74, 75], are used to analyze the contrast agent TIC derived via DCE-MRI to obtain physiological properties such as vessel permeability, blood flow, vessel surface area product, and composition of interstitial space [76–80]. Generation of these increasingly complex pharmacokinetic models is an active area of research and has been used for identifying and subtyping tumor tissue [81–83], lesion characterization [84], and studies of the vasculature [85–88]. Dozens of parameters can be obtained from these pharmacokinetic models, but K_{trans}, v_e, and k_{ep} are most often investigated. K_{trans}, or the volume transfer coefficient, is a constant that describes molecular exchange from blood plasma to extravascular space. It is a function of both permeability and vessel surface area [89, 90]. v_e represents the volume of extravascular space per volume of tissue in which contrast agents accumulate [91]. k_{ep} is a rate constant describing the exchange rate from extravascular space back to blood plasma. These parameters have been directly related to important physiological values implicated in vascular normalization like vessel density, permeability, and size. As such, DCE-MRI is commonly used to investigate the extent of normalization in the tumor microenvironment.

Recently, multiple groups have linked K_{trans} to vascular function and have attempted to show correlations between K_{trans} and markers of angiogenesis like microvessel density (MVD) [92–94]. K_{trans} has been commonly used in vasculature normalization studies as shown by several recent investigations with bevacizumab [95–97]. Chen and Lu et al. showed a significant normalization response and presented evidence for the benefits of a long duration pretreatment to enhance the efficacy of potentially co-administered chemotherapeutics [98]. Pishko et. al similarly showed substantial vascular normalization response, slowed tumor growth, limited increase in edema, and importantly a significant decrease in tumor vessel permeability [96]. Yang et. al were also able to elucidate the relatively short normalization window (1 to 2 days) and showed a significant correlation between values of K_{trans} and k_{ep} with levels of perfusion. As shown in Fig. 2, from Yang and collaborators, the highest levels of K_{trans} and k_{ep} are observed between days 2 and 4 after a single dose of bevacizumab in treatment groups [97]. Increased K_{trans} and k_{ep} are representative of a more normalized vasculature system in these tumors. In another recent study investigating sorafenib and infigratinib, significant K_{trans} changes were associated with diminished tumor growth, mitigation of tumor hypoxia, and a more normal cellular microenvironment [99]. Studies also have reported that decreased levels of K_{trans} as early as 1 day after anti-angiogenic treatment is indicative of positive response in glioma patients [100–102].

While these pharmacokinetic models have shown clinical value, they are limited by their complexity and potentially time-consuming implementation. To avoid these hurdles, certain semi-quantitative values can be obtained in near real-time directly from the time-course of the contrast agent. The common metrics include the initial area under the curve (iAUC), the slope of the steepest portion of the time-course signal, and time-to-peak enhancement. These values can be used individually or in combination with aforementioned quantitative parameters, as shown by Chen and Lu et. al who associated K_{trans} values with significant decreases in iAUC and slope values [98]. In another study of tumor response to bevacizumab, iAUC was implicated as a strong prognostic marker of positive patient response prior to normalization [103]. iAUC, time-to-peak enhancement, and K_{trans} were all shown to correlate with vascular parameters obtained from optical coherence tomography [104]. While not specific to vascular normalization, Zeng and Zhang *et. al*. demonstrated slope, time-to-peak enhancement, and several other semi-quantitative parameters that had significant clinical value in monitoring chemotherapy response [105].

Dynamic susceptibility contrast MRI

Dynamic Susceptibility Contrast MRI (DSC-MRI) also uses gadolinium-based contrast agents but differs from DCE-MRI in that the technique capitalizes on the local inhomogeneities produced from differences in magnetic susceptibility during the first pass of the contrast agent through the body. Large gradients in susceptibility between vasculature and tissue contribute to significantly reduced T2 relaxation times, meaning T2-weighted

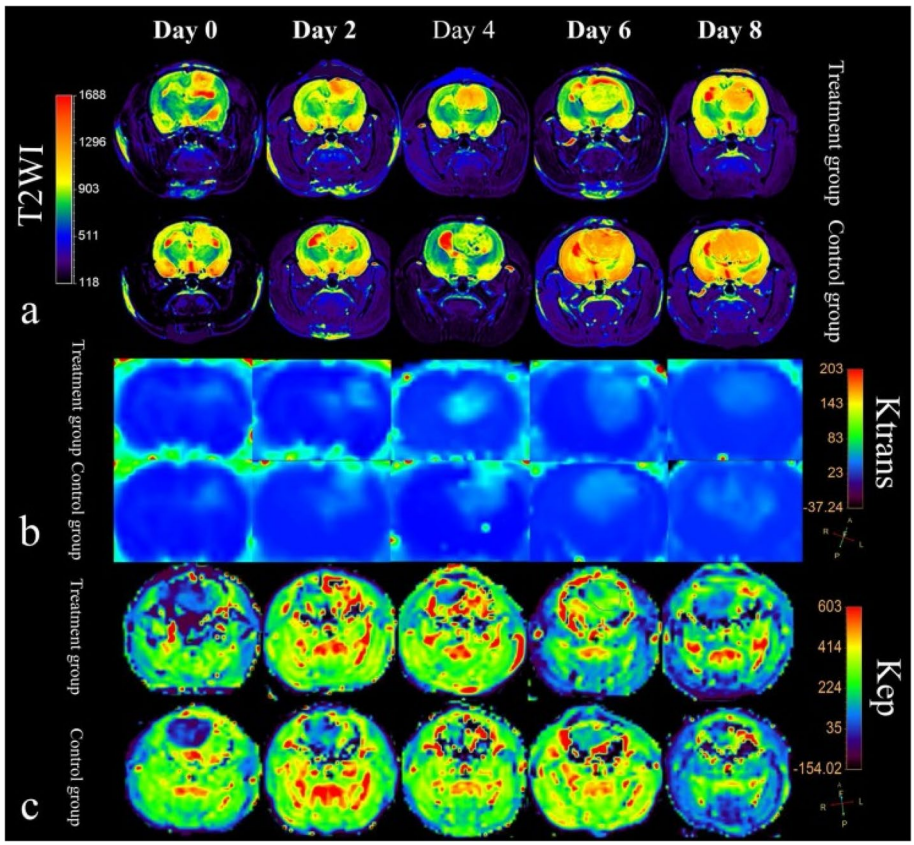

Fig. 2 **a** T2-weighted images of rat brains on days 0 to 8 for treatment (top) and control (bottom) groups. Treatment groups received a single dose of anti-angiogenic bevacizumab on day 0. Shown by regions of higher (more red) T2WI signal, control tumors had higher levels of peritumoral edema than bevacizumab treated tumors on days 2 and 4. Outside of the normalization window, days 6 and 8, edema is restored as tumor growth continues. **b** and (**c**) color maps for DCE-MRI k_{trans} and k_{ep} around tumors from day 0 to day 8. K_{trans} and k_{ep} values are most significantly increased when compared to controls on days 2 and 4, before reducing on days 6 and 8. Increased levels of k_{trans} and k_{ep} are a sign of increased perfusion and a more normalized vasculature. Crucially, these subtle and transient increases help identify this "vascular normalization window" where therapies may be more effective due to this increased perfusion

images show significant contrast enhancement [12, 79, 106–108]. As these gradients are formed due to the localized susceptibility differences between the paramagnetic contrast agent and diamagnetic tissue, the generated signal and overall contrast enhancement are heavily dependent on vessel architecture. The tight junctions prevalent in the blood-brain-barrier make these differences even more pronounced and contributes to the prevalence of DSC-MRI in brain imaging applications [109, 110]. Similar to DCE-MRI, kinetic models can be created based on tracer or indicator dilution theory [111] and allow for the generation of quantitative maps of cerebral blood volume (CBV), cerebral blood flow (CBF), and mean transit time (MTT).

CBV is the fraction of the overall volume occupied by blood and is the simplest to obtain as it is proportional to the integral of the relaxation rate curve. CBF refers directly to the rate of blood delivery to the brain tissue. To estimate the CBF, it is necessary to mathematically deconvolute measures of agent concentration in the tissue of interest and vasculature. MTT is the average amount of time it takes for a single contrast agent to pass through the vasculature. Based on the central volume principle, MTT = CBV/CBF [112]. These blood flow specific parameters coupled with the use of DSC-MRI use for brain imaging, make it an effective choice for investigating vascular normalization in glioma. Relative CBV has been implicated as a potential predictor of biological changes and overall glioma patient response to bevacizumab [113–115] In a recent retroactive study, CBV and CBF were associated with reduced tumor angiogenesis and improved overall survival in bevacizumab-treated patients but had mixed results for the predictive capabilities of the technique [116]. Cho et al. went even further and not only investigated CBV as an indicator of bevacizumab's effect but also connected DSC measurements to a potentially improved patient response when also blocking CCL2, a chemokine implicated in the differentiation

of tumor-associated macrophages [117]. Interestingly, another recent study of bevacizumab in recurrent glioblastoma showed that despite normalization, overall tumor oxygenation worsened [118].

Other MRI-based approaches for monitoring vascular response

DCE-MRI and DSC-MRI are the most common MRI techniques used for investigating vascular normalization, but other MRI techniques have been successfully employed. Intravoxel incoherent motion MRI (IVIM-MRI), which does not require a contrast agent and offers the ability to separate the pure diffusion and perfusion characteristics of water molecules, has the potential to become an effective tool for monitoring normalization [119]. Recently, IVIM-MRI perfusion and diffusion parameters were correlated with pericyte coverage and histological parameters associated with vascular normalization [120, 121]. Blood oxygen level-dependent MRI (BOLD-MRI), which relies on the magnetic susceptibility differences between oxygenated and deoxygenated hemoglobin, also is an attractive option for measuring response to anti-angiogenic therapy without an exogenous contrast agent [122, 123]. Liang et al. combined DCE-MRI-derived K_{trans} values with BOLD-MRI measurements to support the idea that bevacizumab can improve pericyte coverage and increase perfusion [124]. Ma et al. used both IVIM-MRI and BOLD-MRI as a means to investigate a variety of parameters associated with the tumor microenvironment following a combined anti-angiogenic and hypoxia-activated drug treatment regimen [125].

MRI is a powerful medical imaging tool with a wide variety of applications due to its high spatial resolution and lack of ionizing radiation. These advantages in conjunction with the many types of imaging protocols and the ability to co-register functional, molecular, and topographical images make MRI an attractive imaging tool for vascular normalization research. Parameters like K_{trans} and CBF can be directly related to fundamental changes in extravasation, perfusion, diffusion, and overall normalization, which give unique insights to clinicians and researchers alike. A quantitative metric of normalization, the "vascular normalization index", has been proposed that combines multiple parameters including the MR-derived K_{trans} and CBV to provide a metric of normalization that may be a predictor of normalization success and patient survival [126]. However, MRI is commonly associated with long scanning times, high cost, and high sensitivity to motion artifacts. Critically, common MR techniques lack the spatial resolution needed to image vessel at the capillary level. Apart from these common issues, some normalization studies can be hindered by the potentially complex pharmacokinetic models required for analysis and the indirect relationship between commonly investigated parameters and changes observed in the tumor microenvironment. With the availability and the requisite expertise, MRI stands as one of the most useful imaging modalities for vascular normalization studies.

Computed tomography

Computed Tomography (CT) uses x-rays as the basis for image construction. These x-rays attenuate differently as they pass through tissues with varying density in the body, leading to the characteristic contrast difference between skeletal and soft tissue. Iodine-based commercial contrast agents like Iomeprol and Iohexol are often used for soft tissue imaging [127]. X-ray traces are combined and back-projected to form individual 2D tissue slices that can be cycled through and stacked to form a 3D image of the patient [128–131]. The attenuation visualized in these images is directly related to the local concentration of contrast agents in the tissue [132]. Without any further processing, these images already provide considerable structural information, but by monitoring changes in concentration over time it is possible to determine values associated with blood flow and perfusion. This mix of available structural and functional information makes CT a viable option for monitoring vascular response and normalization.

Perfusion computed tomography

Perfusion CT is a form of dynamic contrast-enhanced CT that is commonly employed for vascular imaging and analysis. Similar to the time-course concentration profiles previously described for MR imaging, perfusion CT relies on the creation of time-attenuation curves. Typically, a set of baseline CT images is collected and then compared to a series of images obtained over time after an intravenous bolus injection of contrast agent. From these images, it is possible to relate signal attenuation to the concentration of contrast agent in circulating blood over time [133–136]. These time-attenuation curves can be analyzed or parameters like the slope of the steepest portion, the area under the curve (AUC), mean transit time (MTT), time to peak enhancement, and overall peak enhancement [137], or can be fit to quantitative pharmacokinetic models. Most commonly, the Johnson and Wilson [138] or Patlak [139] kinetic models are employed. These models give a few values that can be more directly related to anatomical and physiological features of the vasculature in the tissue or organ of interest. Regional blood flow (BF) and blood volume (BV) provide values for the flow rate and total volume of blood in the imaging region. The extraction fraction (EF) describes the fraction

of contrast agent that is transferred to the extravascular space during a single passage. The permeability surface area product (PS) describes the total diffusion-based flux across the capillaries, similar to the K_{trans} value obtained via MR imaging. Also available through further processing are maps for arterial perfusion (AP) and perfusion index (PI). Overall, this collection of parameters gives insight into oxygen delivery, vessel leakage, and vessel density, and these parameters could be monitored longitudinally to identify the vascular normalization window.

Due to its widespread availability and reproducibility, perfusion-CT has been used extensively in clinical applications of anti-angiogenic agents [140–144]. Perfusion-CT's ability to elucidate parameters directly related to vasculature function makes it a powerful prognostic tool for patients [145–147]. Zou *et. al* were able to correlate a variety of factors including AP and PI to MVD and VEGF expression levels, allowing for improved differentiation of benign and malignant lung lesions [147]. It has been shown that after a single cycle of treatment, BF and BV could help predict patient response to anti-angiogenic agents [148]. Jiang et. al. not only showed a significant reduction in BF, BV, and PS and significant increases in MTT after anti-angiogenic treatment but also connected these parameters back to patient response [149]. Kambadakone et al. demonstrated that perfusion-CT could be used to detect a positive tumor response to bevacizumab and radiotherapy by capturing significant reductions in BF and BV, which correlated with changes in tumor MVD [142]. Heist et al. provided further support for a vascular normalization window by showing that a standard dose of bevacizumab significantly reduced BF, BV, and PS, indicative of an overall drop in perfusion. Instead of completely impairing vasculature, greater survival benefits may be related to improved perfusion through tumor vasculature [143]. PS also has been shown to correlate with values obtained for K_{trans}, making perfusion-CT a potentially attractive option in situations where MRI is unavailable [150].

Dual energy computed tomography

Dual Energy CT (DECT), also known as Spectral CT, is a recent advancement on conventional CT that relies on gathering data from two or more peak energies following the injection of a contrast agent, typically iodine. This is done by tracking attenuation from two different tube voltages, typically one low (~70 keV) and one high (~140 keV). DECT uses advanced sensors and software to combine these separate acquisitions creating richer and more complex images [151–154]. Along with the slope of the attenuation curves, the most common method for analyzing DECT images is to track the iodine concentration (IC) obtained from iodine maps. As the iodine maps show the degree of vascularization in the imaged tissue, the volumetric uptake of iodine can be representative of tissue perfusion. DECT also offers substantial benefits over conventional CT angiography with superior temporal resolution [155, 156] lower radiation dose [157], and easier differentiation of vascular tissue from the background [158].

While not entirely interchangeable, DECT is a viable and potentially superior alternative to conventional contrast-enhanced CT. Several groups have reported a good correlation between metrics like BV, BF, and MTT from perfusion CT with ICs from DECT in a variety of cancer types [159–162]. Additionally, DECT was shown to provide a significant improvement over conventional imaging and classification techniques specifically when evaluating the anti-angiogenic response to bevacizumab [163]. In another bevacizumab-focused study, Han et al. reported that the slope of the energy spectrum curve and the IC over time correlated positively with changes in tumor size as well as VEGF and HIF-1a expression levels [164]. Separate studies into four different tyrosine kinase inhibitors provided evidence that DECT can be employed for early prediction of patient response. More specifically, studies into axitinib [165], sunitinib [166], regorafenib [167], and sorafenib [168] demonstrated that normalized IC values could be predictive of a favorable response and that the parameters related to IC, such as volumetric iodine-uptake, can be more sensitive in the early detection than other CT methods.

Micro-computed tomography

Perfusion-CT and DECT are the most commonly employed types of CT for monitoring vascular response to therapy due to their clinical availability, speed, and high resolution, but micro-CT has been applied in some research settings outside of clinical applications. Briefly, micro-CT uses very similar technology to conventional CT, but at a much smaller scale and with enhanced resolution [169]. This means micro-CT cannot be used clinically but does have a wide array of applications for small animal models and ex-vivo samples [170] including monitoring vascularization and the effects of anti-angiogenic treatment [171]. Gu et. al capitalized on the enhanced resolution of micro-CT to demonstrate a significant drop in relative vessel density for vessels smaller than 50 microns [172] following anti-angiogenic therapy while Hutchenreuther et. al were able to use micro-CT to investigate the role of cancer-associated fibroblasts and the CCN2 pathway in tumor neovascularization [173]. Micro-CT is often characterized by the impressive 3D reconstructions it can generate, and while it cannot be used clinically these information-rich reconstructions

make micro-CT a valuable modality for investigating micro-vasculature.

Overall, CT is a vital imaging tool across the medical field that has structural, functional, and molecular imaging capabilities. CT is available in most clinical settings, is repeatable, and provides high resolution with short scanning times. With a multitude of methods and scanners, there are many ways in which CT can be utilized to characterize the response of vasculature to anti-angiogenic therapies. Qualitative parameters associated with contrast agent delivery and more quantitative parameters related to blood flow and perfusion can be obtained and tracked well with physiologic responses in patients. One of the main drawbacks of CT is the use of ionizing radiation, which can limit the frequency of imaging trials and is potentially harmful to patients. CT images also are sometimes susceptible to a variety of artifacts that can obscure tissues of interest. Nonetheless, CT remains one of the most commonly employed tools for investigating the tumor microenvironment and is a very good option for monitoring vascular normalization.

Positron emission tomography imaging

Positron Emission Tomography (PET) is used for sensitive and quantitative molecular imaging of cells and tissues. PET imaging is based on the detection of the radiation emitted from a radiolabeled tracer administered systemically [174]. The radiolabeled tracers are designed to bind with specific biomolecules involved in disease progression or treatment response. To date, various PET tracers have been produced for the assessment of various diseases [175–177], particularly in cancer [178, 179]. For example, 2-deoxy-2-[18F]-fluoro-D-glucose (18F-FDG PET) can be used to detect tumors based on their elevated glucose metabolism [180, 181], whereas 3′-deoxy-3′-18F-fluorothymidine (18F-FLT) PET detects tumors based on increased DNA replication [182].

Targeted contrast agents also have been engineered for PET-based molecular imaging of tumor angiogenesis. For example, $\alpha_v\beta_3$ and $\alpha_v\beta_5$ integrins are heterodimeric transmembrane glycoproteins overexpressed in newly formed vessels. Arginine-glycine-aspartate (RGD) specifically binds to $\alpha_v\beta_3$ integrins and has been conjugated to radiotracers for PET-based molecular imaging of angiogenesis [183–185]. The dimeric or polymeric RGD peptides demonstrate superior binding affinity for $\alpha_v\beta_3$ in comparison to their monomeric counterparts [186]. Thus, RGD peptides labeled with various isotopes such as ^{18}F, ^{68}Ga, and ^{64}Cu have been evaluated as tracers for $\alpha_v\beta_3$ integrin PET imaging. ^{18}F RGD-K5 in particular has been used in clinical studies to image angiogenesis on various types of cancer including breast cancer, lung cancer, head and neck cancer, and lymphoma. Radiolabeled RGD has been used to study the relationship between angiogenesis and tumor blood flow [187]. However, laborious labeling procedures and low yields have hindered the clinical translation of PET tracers. Synthesis of improved RGD tracers for PET imaging is continuously being pursued. Guo *et. al* reported a one-step RGD labeling procedure to prepare [18F] AIF-NOTA-PRGD2 and compared its kinetic parameters with well-established RGD tracers, [^{18}F]FPPRG and [^{68}Ga]Ga-NOTA-PRGD [188]. [^{18}F] AIF-NOTA-PRGD2 demonstrated comparable binding affinity to the aforementioned radiotracers; however, the agent showed high uptake which may be due to nonspecific accumulation and a lower clearance rate [188]. [^{18}F] AIF-NOTA-PRGD2 also has been used in a clinical trial to evaluate the activity of apatinib, an antiangiogenic agent [189].

Recently in a similar study, aminopeptidase N receptor (APN/CD13) was used as a biomarker of angiogenesis [190]. APN/CD13 is highly expressed in angiogenic blood vessels and correlates well with cancer progression. Asparagine-glycine-arginine tripeptide sequence (NGR) has high selectivity for APN/CD13 [191] and has been investigated as a tracer for PET imaging where scientists introduced a lactosamine derivative to NGR that binds with galectin-3, also overexpressed in certain cancer types, to develop a dual-targeting tracer [190].

The PET tracer [18F]-FMISO binds to the macromolecules in hypoxic tissue enabling detection by PET. [18F]-FMISO uptake by hypoxic tissue has been verified by biological markers on a molecular level (Fig. 3) [192]. In one study, hypoxia was used as a surrogate parameter, to identify and trace vascular normalization using an 18F-misonidazole [18F]-FMISO [193]. Hypoxia collectively stems from increased interstitial pressure, edema, and altered metabolism, as a result of abnormal vasculature. Therefore, hypoxia has been used as an indirect measure of vascular normalization. In this study, dovitinib, a multi-targeted tyrosine kinase inhibitor was used for anti-angiogenic treatment followed by chemotherapeutic drugs. Tumor uptake of FMISO corresponds to hypoxia and was a proxy for the identification and tracking of vascular normalization. In a phase II randomized trial, [18F]-FMISO was used to evaluate the benefits of a novel multi-tyrosine kinase inhibitor, nintedanib, combined with the chemotherapeutic drug, paclitaxel [194]. PET-based detection of [18F]-FMISO was used to evaluate interstitial oxygenation levels as a measure of vascular normalization and to determine whether to continue administering nintedanib.

Prostate-specific membrane antigen (PSMA), a protein highly overexpressed on prostate cancer endothelial cells, is another biomarker used in PSMA-PET imaging for staging and restaging prostate cancer [195].

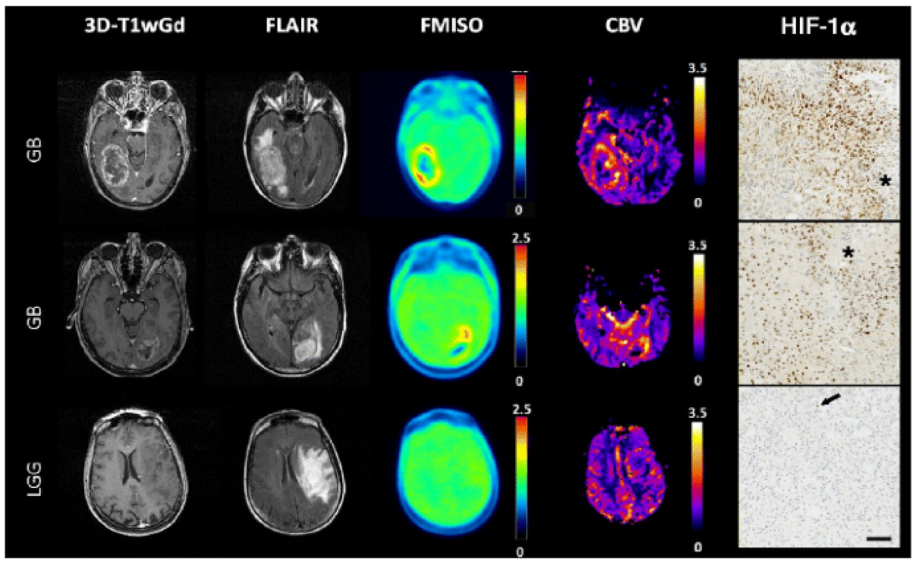

Fig. 3 Three dimensional T1 weighted gadolinium (3D-T1wGd) injected MRI image, Fluid attenuated inversion recovery (FLAIR) image. F-MISO, cerebral blood volume map, and HIF-α immunostaining images of two patients with glioblastoma (GB) and low-grade glioma (LGG). GB patients showed enhanced contrast and necrosis in the MRI image, hyperintensity in the FLAIR image, high F-MISO uptake and higher CBV intensity whereas no contrast enhancement or F-MISO uptake was observed in patients with LGG. These results were further validated with HIF-α immunostaining in which high nuclear expression of HIF-α was observed in GB shown by asterisks and minimal to no HIF-α expression in LGG. Scare bar: 500 μm [191]

Although first characterized in the prostate, PSMA is also expressed in the neovascular endothelium of non-prostate solid tumors while there is little to no expression in normal vascular endothelial cells. This variable expression makes PSMA a potential molecular target for diagnosis and therapy in other malignancies such as breast cancer [196, 197], colorectal cancer [198, 199], renal cancer [200, 201], glioblastoma multiform [202, 203], thyroid cancer [204, 205], pancreatic cancer [206], hepatocellular cancer [207] and others [195, 208, 209]. Increased PSMA expression can be used as a surrogate for increased tumor angiogenesis in cancer, which is associated with poor patient prognosis. For example, PSMA upregulation is associated with lower overall survival, higher tumor size and cell proliferation in breast cancer, and higher histologic grades in non-small cell lung cancer. PSMA has been used for determining the aggressiveness of various types of cancer [210] and for differentiating malignant tumors from benign [206] based on changes in tumor vasculature.

^{18}Fluoride (^{18}F) and ^{68}Gallium (^{68}Ga) are common isotopes used to label PSMA antigen ligands [211, 212]. (^{18}F) F-DCFPyL [213] and Glu-NH-CO-NH-Lys-(Ahx) also known as 68Ga(HBED-CC) or ^{68}Ga-PSMA-11 gozetotide are FDA-approved diagnostic radiotracers for PSMA-PET imaging for prostate cancer [214, 215]. Recent studies have used ^{68}Ga-PSMA-11 and (^{18}F) F-DCFPyL to diagnose or stage non-prostate cancers by leveraging neovascular PSMA expression. For example, ^{68}Ga-PSMA-11 was used to detect and stage renal carcinoma. In this study, PSMA-PET enabled the detection of sub-centimeter lesions which is challenging with other standard imaging systems like CT and MRI. Likewise, (^{18}F) F-DCFPyL radiotracer was used to localize metastatic differentiated thyroid cancer by detecting angiogenesis within the tumor [216].

^{68}Ga isotope is widely used for labeling PSMA ligands for PSMA-PET imaging. However, ^{18}F may be preferable due to shorter positron range, higher positron yield, and economic practicality [217, 218]. Furthermore, the accumulation of ^{68}Ga in the urinary bladder could mask the presence of a lesion in the prostate or prostatic bed resulting in a false negative diagnosis.

One of the major limitations of PSMA-PET is the non-specific expression of PSMA in normal tissues such as salivary glands, renal tubules, small intestines, the brain, liver, spleen, etc. Moderate to intense uptake of PSMA radiotracers in various organs has been observed. Retaining these tracers in different organs makes interpreting PET images challenging and may hinder the clinical diagnostic outcome. Additionally, histopathological studies indicate significant inter and intra-heterogeneity in PSMA expression among various cancer types. In parts, significant discrepancies may be attributed to different techniques and products used in the analysis [208]. Due to the lack of a standardized quantification method, it is

difficult to determine PSMA availability for PSMA-PET imaging.

PET imaging can be performed as static or dynamic scanning. Static PET imaging provides a spatial map of regional tracer concentration whereas dynamic PET scanning provides both temporal and spatial information of the tracer [219]. Visual inspection and standardized uptake value (SUV) are used regularly for image interpretation in a static PET imaging system in a clinical setting. SUV is a semiquantitative approach and is the ratio of the radiotracer concentration in a region of interest and the injected activity divided by normalization factors such as body weight, body surface area, and lean body mass [220]. Static PET was used to monitor vascular normalization following treatment by tyrosine-kinase inhibitor, dovitinib [193]. The SUV quantification method does not require arterial cannulation and has a shorter scanning time, making it a cheaper and more patient-friendly alternative to dynamic PET imaging. However, SUV approximation does suffer from significant variability introduced by slight differences in experimental procedure [220]. Dynamic PET enables the measurement of tracer kinetics and provides mean tissue radioactivity as a function of time. The compartmental modeling approach is considered the gold standard in PET imaging to quantify the kinetics of tracers. However, it requires complex dynamic data acquisition and arterial blood sampling. Other analysis methods used for oncological PET imaging include the Logan plot and the Patlak plot. The Logan and Patlak plots are widely accepted methods for reversible and non-reversible tracer kinetic analysis. Although, dynamic PET provides superior information in comparison to conventional static PET, its clinical application is hampered due to duration of the protocol and limited axial field of view (FOV). However, new generation PET/CT equipped with an extended FOV and sophisticated software packages are expected to significantly contribute in oncological diagnostics [221].

To summarize, PET is highly sensitive for molecular and functional imaging of vasculature. PET Imaging allows for the detection of isotopes in target tissues at picomolar concentrations. However, the anatomical resolution of PET is limited to 1-2 mm^3 in small animal imaging systems and 4-8 mm^3 in clinical imaging systems. This requires PET to be aided by CT or MRI to improve anatomical resolution [222]. Furthermore, PET imaging is highly dependent on the binding affinity of tracers and the expression of target receptors in blood vessels. While the toxicity of radiotracer is mitigated by the use of picomolar concentrations, the low-yield labeling procedure is the major challenge in the synthesis of radiotracers.

Optical imaging

Optical imaging refers to a broad family of techniques that uses light and leverages the properties of photons to investigate tissues and cells. Optical imaging is minimally or non-invasive and can achieve sub-cellular resolution. Various optical imaging methods such as optical coherence tomography angiography, optical tomography, and confocal laser endoscopy can be used to image vasculature in clinical settings for diagnosing an assortment of diseases and monitoring vascular response to treatment.

Optical coherence tomography angiography

Optical coherence tomography angiography (OCTA) is a noninvasive method for imaging blood flow in the retina and choroid. OCTA shares similarities with optical coherence tomography (OCT) imaging. Both methods operate on the principle of interferometry, generating images by measuring differences in the amplitude and delay of light that has been reflected or backscattered by the sample [223]. While OCT directly measures structural information, OCTA detects vasculature by the motion contrast created by circulating blood cells. The movement of blood cells in vasculature produces shifting signals in successive scans of the same region and is distinguished from the unchanging signals produced by static features [223, 224].

OCTA has been used to successfully identify abnormal vasculature in the squamous epithelium of the cornea and conjunctiva, choroids, and skin [225–228]. OCTA was used in a study to evaluate the effectiveness of topical treatments for patients diagnosed with ocular surface squamous neoplasia (OSSN) and were presenting tumors [225]. OCTA images were taken to assess tumor vasculature at three time-points: before treatment, at mid-treatment, and post-treatment during tumor resolution. OCTA allowed for changes in vessel area density in the tumor to be monitored with treatment. In another study, OCTA was used to evaluate the vascular structure of choroidal neovascularization (CNV) in patients that had been treated with multiple injections of VEGF. This allowed for the identification of common vascular features in CNV [226]. While OCTA is primarily used for imaging eyes, preliminary studies have been completed for imaging capillaries in skin [227, 228]. Deegan *et. al.* used OCTA to demonstrate structural differences in microvasculature among numerous skin conditions and in comparison to healthy skin [227].

A major advantage of OCTA is that it produces depth-resolved images and can visualize microvasculature (i.e., capillary networks). OCTA also benefits from not requiring the use of contrast dye. However, some drawbacks include limited quantitative information about blood flow, the inability to determine alterations in vascular

permeability or detect vascular leakage, and image artifacts that potential may lead to misinterpretation of the images with respect to vascular biology [224]. Furthermore, OCTA has limited imaging depth, and therefore, is restricted to superficial tissues.

Optical tomography

Optical Tomography (OT) is an optical imaging technique that measures the scattering of near-infrared (NIR) diffused light in tissue. NIR source wavelengths are in the range of 700-900 nm. Concentrations of oxygenated and deoxygenated hemoglobin can be determined from the measured optical absorption, which provides information on the vascularity of a region [229]. Hemoglobin concentrations can indicate tumor angiogenesis, a marker of tumor growth or metastasis, as well as tumor hypoxia, which can correlate to tumor response to therapeutic treatment [230–232]. OT has high temporal resolution but suffers from limited spatial resolution. Thus, an additional imaging modality, such as ultrasound (US) or magnetic resonance imaging (MRI), often times is used in conjunction with OT to provide additional spatial information.

With localization and structural information provided through US or MRI, OT has been used in clinical studies to characterize, diagnose, and monitor the hemoglobin and oxygen levels of cancerous and noncancerous breast lesions [230, 231, 233]. Zhu *et. al*. studied the hemoglobin distribution and blood oxygen saturation levels in US-visible breast lesions clinically and demonstrated the utility of OT with US to monitor tumor vascular response to chemotherapy [8, 9, 230, 231]. Another study of breast lesion used MR images to provide structural information that were overlaid with OT images during analysis. Blood oxygenation and hemoglobin concentration values were calculated to investigate the oxy- and deoxyhemoglobin content of the lesions and used to characterize the different lesion types [233]. In a separate study, OT was used to detect the difference in perfusion-related parameters within days following treatment with an anti-angiogenic agent in responding and non-responding cell lines [234]. By detecting and monitoring hemoglobin and oxygen levels to glean vascular density information, OT offers metrics with the potential to help predict clinical outcomes in breast cancer patients.

Albeit high temporal resolution, the lack of sufficient spatial resolution limits its application as a standalone imaging technique and requires OT to be combined with other imaging modalities.

Confocal laser endoscopy

Confocal laser endoscopy (CLE) operates on the principles of confocal microscopy, which is a fluorescence imaging technique that illuminates tissue with a low-power laser and collects reflected, in-focus light through a pinhole spatial filter. Currently, there are two types of CLE. One is probe-based, consisting of confocal mini-probes in the accessory channel of an endoscope. The other is endoscope-based, where a confocal scanner is built into the tip of the endoscope [235].

CLE has been used to identify irregular vasculature associated with carcinoma in the colon, liver, bladder, stomach, and esophagus [236–239]. When using CLE for examining the tumor mucosa, De Palma *et. al*. found that blood vessels in tumor tissues were more dilated and tortuous, with higher branching, leakage, and abnormal blood flow compared to normal tissue [236]. A study that used CLE for examining gastric cancerous mucosa found that undifferentiated gastric cancers exhibited hypovascularity, with abnormal, short branch vessels, while differentiated gastric cancers were hypervascular and tortuous with varied shapes and diameters among the microvessels [237]. The same study also investigated esophageal carcinomas with CLE and found dilated and/or abnormally tortuous vessels in the mucosa with unusual variability in shape and size [237]. A study of lesions in the liver identified vascular patterns associated with neoplasia with 86% accuracy [238]. A CLE study of the urothelial carcinoma associated distorted vasculature with high-grade cancer [239]. Across these studies, CLE has demonstrated diagnostic potential through vascular imaging of various carcinomas.

Although, CLE has been primarily used to histological evaluation of gastrointestinal system, Confocal laser endomicroscopy has been investigated to evaluated vascular networks in fresh biopsies of malignant colorectal tissue. This technique demonstrate potential application in clinical setting for monitoring anti-angiogenic therapy [240]. Advantages of CLE include having a high spatial resolution, allowing for the detailed evaluation of vascular structure at cellular level. Some drawbacks, however, include limited imaging depth and the need for a contrast agent (i.e., fluorescent dye such as fluorescein) to be administered topically or intravenously [235, 241].

Multi-photon microscopy

Multi-photon microscopy (MPM) is an optical imaging technique that can be used to visualize vasculature *in vivo*. MPM uses one or more long-wavelength coherent laser source to excite a fluorophore using two or more photons, each photon carrying a fraction of the energy that is required for single-photon excitation.

MPM has been used to investigate morphometric details of excised blood vessel walls [242]. MPM has been used to study tumor vasculature in conjunction with surrounding cells to create a wholistic image

of the tumor microenvironment [243, 244]. Brown *et. al*. used MPM to study the relationship between VEGF and angiogenesis in tumors, quantify tumor blood flow with red blood cell velocity measurements in tumor vessels, and quantify the permeability of tumor vessels *in vivo* [243]. Recent advances in MPM for tumor vascular imaging include the design and exploration of new dyes, such as AIE luminogen (BTPETQ), which was shown to improve imaging depth and signal-to-background ratio, and Pluronic® fluorescent nano micelles, which were found capable of imaging leaky tumor vessels [245, 246]. Other particles have been created for imaging and photodynamic therapy (PDT), which allows for two-photon imaging of vasculature concurrent PDT treatment [247, 248]. Additionally, multi-photon luminescence imaging of gold nanoparticles as a contrast agent has been used to investigate monitor vascular permeability in mouse brain in vivo [249]. MPM recently has also been used to track gold nanoparticles within vasculature, unleashing the potential to obtain real time structural and functional information of vasculature *in vivo*, which is essential to monitoring vascular changes during and post treatment [249]. Recently two-photon laser scanning microscopy (TPLSM) equipped with Bessel focus module was used to capture volumetric hemodynamics in live mice at a spatial and temporal resolution that can be used to obtain structural and functional information of blood vessels (Fig. 4) [250]. With such extensive work done in animals *in vivo*, MPM shows potential as a future technique for clinical evaluation of tumor vasculature.

MPM is advantageous over confocal imaging in that the excitation is focused to a spot, with minimal background fluorescence created or collected, which reduces the risk of phototoxicity. The use of long excitation wavelengths also allows for deeper imaging of tissue. A major disadvantage of MPM is the risk of thermal damage to the subject during imaging, although this can be avoided with careful and proper use of the laser at appropriate power levels [243, 251]. Similar to other optical imaging methods, MPM also suffers from limited imaging depth.

Ultrasound imaging

Ultrasound (US) is a clinical imaging modality that has been investigated for the assessment of various diseases such as rheumatoid arthritis [252], inflammatory bowel disease [253], cardiovascular disease [254, 255], and various types of cancer [256–258]. In general, ultrasound is a non-invasive and safe diagnostic imaging modality that offers many advantages including affordability, accessibility, and shorter scan time. In addition, ultrasound provides superior soft tissue contrast and relatively deep imaging depth. B-mode US imaging is the

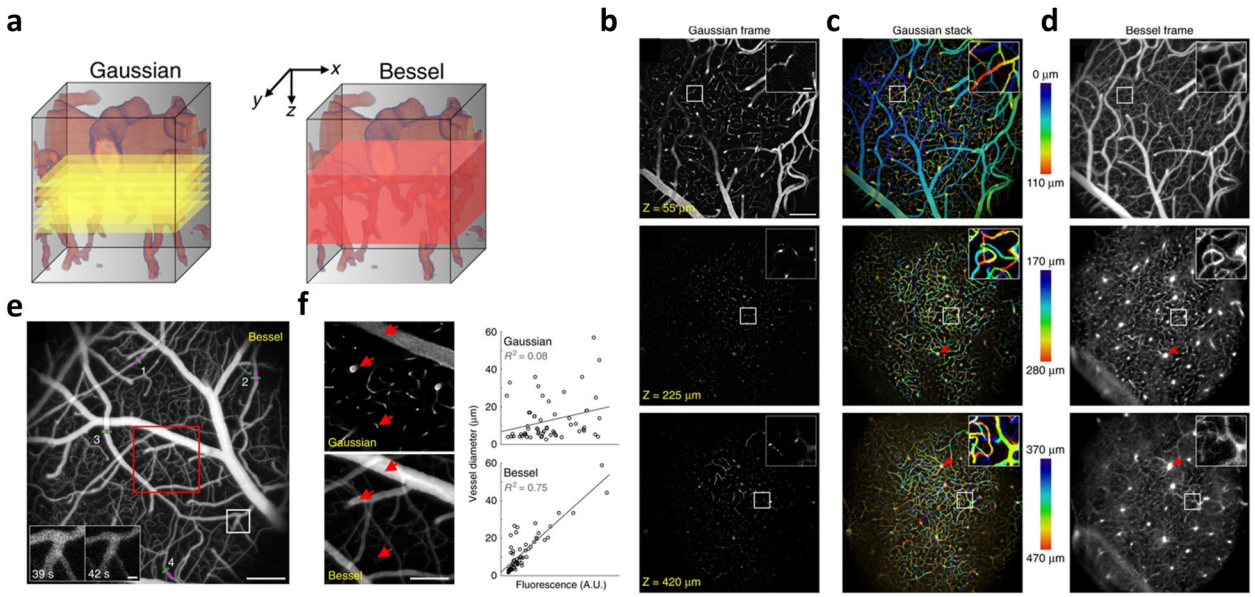

Fig. 4 **a** Schematic illustration of Gaussian and Bessel volumetric TPLSM. Gaussian volumetric imaging is acquired using 2D images taken at multiple Z-positions whereas Bessel volumetric image is acquired in a single frame within the volume defined by the 2D scanning area. **b** Gaussian images of vasculature acquired with Texas Red labeled dextran at different depth (Z= 55µm, 225 µm and 420 µm) (**c**) Depth-dependent color-coded Gaussian image stacks within 0-110 µm, 170 – 280 µm and 30 – 470 µm. **d** A 100 -110 µm thick Bessel frame acquired within the volume of (**c**). **e** A grayscale vasculature image acquired with Bessel TPLSM. Insets represents the zoomed-in views of the whiteboxed region showing changes in vessel size at 39 s and 42 s. **f** Gaussian frame at Z= 50 µm and Bessel images of the red-boxed region in (**e**) captured at different times. Red arrows indicates large, medium and small vessel for comparison between Gaussian and Bessel TPLSM [249]

most commonly used technique and serves as the basis for ultrasound imaging. This involves the transmission of ultrasound pulses and the collection of reflected echoes by the ultrasound transducer. As the sound waves propagate through tissue, a fraction of the transmitted waves is reflected depending on the acoustic impedance of the tissues. The varying amplitude of US echoes collected by the transducer is then translated to pixel intensity to allow visualization and quantification of anatomical structures. In a clinical setting, B-mode imaging is used to identify cysts, lesions, tumors, and other structural or functional anomalies. While regular B-mode imaging is limited to identifying anatomical features, contrast-enhanced dynamic US imaging enables functional imaging of vasculature. Contrast-enhanced US imaging has been utilized to monitor changes in tumor perfusion and blood flow during tumor progression or antiangiogenic therapy.

Contrast-enhanced US imaging

Contrast-enhanced US imaging (CEUS) has dramatically broadened the scope of US imaging through the application of contrast agents. CEUS has demonstrated higher detection sensitivity via signal enhancement and high temporal resolution. Microbubbles are the most common contrast agent used for CEUS. Microbubbles are core-shell particles with a gas core and either lipid or albumin shells that are typically 1-4 μm in diameter. There are many commercially available microbubbles such as Optison, Definity, Sono Vue, and USphere, a few of which are already FDA-approved. The gas core, which is usually biologically inert, determines the stability of microbubbles, for example, perfluorocarbon gas cores generate sufficiently stable microbubbles [259]. Microbubbles have a high echogenicity and can generate a strong acoustic signal in an acoustic field as a result of radial oscillation, which exceeds the amplitude of the acoustic waves reflected by tissue interfaces [260]. The stability and signal amplitude of the microbubbles depends on the properties of the gas core, the overall size of the bubbles, the nature of the surrounding medium, and the frequency and power of the incident ultrasound echo. Hemodynamically, microbubbles are identical to red blood cells. At the steady state, the enhancement in acoustic intensity is directly proportional with the microvascular blood volume. For perfusion imaging, a high-amplitude ultrasound pulse is transmitted to burst microbubbles flowing through a tissue volume of interest. The tissue volume is replenished with circulating microbubbles, and the rate of increase in echo intensity provides important information with respect to the extent of vascular perfusion in the tissue of interest blood velocity, the product of two provides microvascular perfusion measurement [260, 261].

CEUS has been used to evaluate the therapeutic outcome of cancer treatment by monitoring tumor angiogenesis [262]. Moreover, microbubbles can be targeted to tumor vasculature for localized monitoring of vascular changes [263]. In one recent study, CEUS was used to trace oxygen-microbubble (O_2-MB) induced vascular normalization [19]. In this study, microbubbles were fabricated with various volume ratios of oxygen and perfluoropropane (C_3F_8). The O_2-MBs were used as an oxygen delivery vehicle and C_3F_8 microbubbles were used as a contrast agent to evaluate tumor perfusion. An increase in tumor oxygenation achieved through external US stimulation led to inhibition of Hypoxia-inducible factor 1—alpha (HIF-1α) expression (Fig. 5a), which further reduced VEGF transcription and mitigated tumor angiogenesis [264]. O_2-MBs may induce vascular normalization without decreasing vascular density unlike anti-angiogenic agents, which may result in vascular regression [19]. The pre- and post-C_3F_8-MB injection images were quantified to evaluate tumor perfusion (Fig. 5b). Following treatment with O_2-MBs, C_3F_8-MBs were infused via an injection pump with a velocity of 0.3 ml/h to maintain the vascular concentration of C_3F_8-MBs during ultrasound contrast imaging. The administration of O_2-MBs led to higher perfusion, which resulted in better drug delivery to established tumors in comparison to control and C_3F_8-MBs.

Dynamic contrast-enhanced ultrasound

Dynamic contrast-enhanced US (DCE-US) is a multiparametric functional imaging technique that can be used for quantitative imaging of tumor perfusion [265]. DCE-US imaging has further advanced US diagnosis through digitized quantification of contrast uptake on recorded video data. In general, for DCE-US, a high dose of ultrasound contrast agent is injected followed by an immediate flush with normal saline. The images are recorded for 3 minutes following injection and analyzed to evaluate treatment response. DCE-US allows more accurate characterization of tumor vascularity than conventional B-mode US and has been successfully used for angiogenesis quantification in cancer patients [266, 267]. DCE-US is used to evaluate quantitatively blood flow and blood volume as measures of perfusion [268, 269]. Parameters such as mean transit time, peak intensity, time to peak contrast intensity, wash in time, washout time, and slope of the contrast wash are collectively used to evaluate therapeutic outcome [262]. Additionally, the contrast-enhanced ultrasound intensity can be plotted as a function of time and the AUC can be calculated. Studies have shown that a significant drop in AUC reflects a detectable

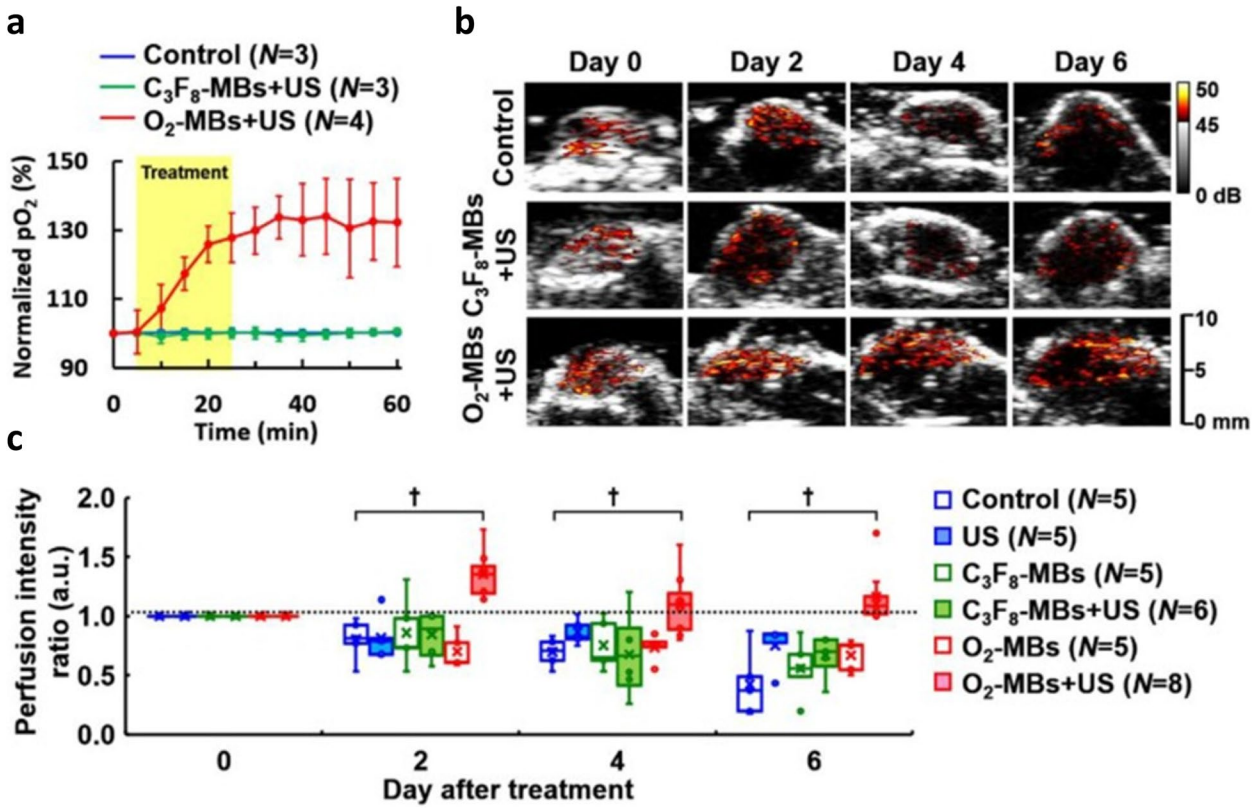

Fig. 5 Enhanced tumor perfusion through oxygen delivery. **a** Normalized partial oxygen pressure in the control group tumor, and tumor treated with C3 F8 and O2 microbubbles. **b** Change in blood perfusion traced at different time points using US contrast imaging. **c** Graphical representation of perfusion intensity at different time points [264]

change in tumor perfusion [268, 270] and thus, can be used as an image-based metric for monitoring treatment outcomes in cancer [271–273].

DCE-US provides superior temporal resolution which enables real-time microvessel perfusion and repeatable short examinations. DCE-US offers crucial insights into the heterogeneity of tumor vascularization that correlates well with standard histological measures; however, vessel structural features are difficult to resolve with this technique due to the limited spatial resolution [274]. Another major challenge with DCE-US imaging is the limited circulation time of microbubbles. The circulation half-life of microbubbles following intravenous injection is less than 7 min [275] which limits the image acquisition time window. Nevertheless, DCE-US serve as a viable image-based option for determining the "normalized window" for anti-cancer therapies.

Acoustic angiography

Acoustic angiography is a CEUS imaging approach that is used for high-resolution microvascular imaging [276]. Acoustic angiography is performed using dual-frequency transducers with non-overlapping bandwidths. The "transmit" transducer has an operating frequency close to the resonance frequency of the microbubble contrast agents and transmits pulses to drive nonlinear bubble oscillations. The "receive" transducer has an operating frequency that is a harmonic of the transmit transducer and receives superharmonic emissions radiated by the microbubbles [277]. Because tissue is not a strong source of nonlinear acoustic emissions, acoustic angiography images can be constructed with a high contrast-to-tissue ratio. Using a high frequency transducer as the receiver allows for construction of high resolution images. This imaging modality provides high-resolution three-dimensional maps of microvasculature with little tissue background and can resolve 100-200 μm diameter vessels up to to a depth of approximately 150 mm [278, 279]. Acoustic angiography has been used as a diagnostic tool to identify tumors and monitor changes in vessel morphology and densities [279, 280]. For example, the modality has been used to detect changes in microvasculature density following radiotherapy of cancer [281]. Recently, arterial labeling US subtraction angiography has been developed, utilizing PFC nanodroplets for imaging single blood vessels [282]. Acoustic angiography can be

combined with DCE-US imaging to monitor changes in the structure and function of microvasculature during cancer treatment and potentially predict clinical outcome [283].

Acoustic angiography offers a cost-efficient and non-invasive tool for monitoring morphological changes in tumor vasculature indicative of a positive tumor response to therapy. For example, Rojas et al. demonstrated that acoustic angiography could detect changes in vascular density following antiangiogenic and Notch inhibition therapies one week prior to a reduction in tumor volume [284]. The combination of acoustic angiography with functional ultrasound imaging such as DCE-US could be an effective approach to evaluate and monitor vascular normalization. The major challenge in acoustic angiography, however, is the availability of dual-frequency transducers that can both transmit low-frequency signals and be able to detect harmonics at higher frequencies. There are ongoing efforts to meet this need by developing new dual-frequency transducers [285–287].

Doppler US imaging

Doppler US imaging methods are well-established tools for real-time quantitative analysis of blood flow and are heavily used in clinical diagnosis. Tumor blood flow can be abnormally slow and fluctuate with time, and in some cases can be stagnant or reverse direction [288]. Quantitative measurements of blood flow and directionality, along with vessel structural details, can provide crucial insight into the response of tumor vasculature to antiangiogenic therapy. There are multiple formats for Doppler sonography, including spectral Doppler, color Doppler, and power Doppler. Each format will be described briefly along with their advantages and disadvantages with respect to interrogating and displaying blood flow.

There are two versions of spectral Doppler: Continuous-wave Doppler (CWD) and Pulsed-wave Doppler (PWD). In CWD, ultrasound waves are transmitted and backscatter from flowing cells are received continuously and used to estimate the velocity along a user-defined path. CWD is ideal for analyzing high velocity blood flow, which is observed frequently in vascular pathologies (i.e. atherosclerosis). A major disadvantage of CWD is the inability to determine where the velocities are estimated along the user-defined path. Unlike CWD, PWD sends short pulses (<30 cycles) of sound repeatedly and alternates between emission and reception of ultrasound signal. PWD offers gating in which users can define a small area where the Doppler shifts are recorded and allow the estimation of blood velocity at a specific location. However, estimates of blood velocity are less accurate with PWD for high velocity flow and at greater distances from the transducer. It is important to note that spectral Doppler plots flow velocity as a function of time separate from an ultrasound image. Other Doppler modalities, such as color and power Doppler, create spatial maps of blood flow that can be combined with B-mode images of the tissue and vasculature.

Color Doppler is the color-coded visualization of average velocity and direction in the region of interest defined by the user. In color Doppler, blood flowing away from the transducer is represented as blue while blood flowing towards the transducer is represented as red. However, similar to PWD, when a Nyquist limit is reached (f=PRF/2), Doppler shifts cannot determine accurately the flow direction and velocity. Compared to color Doppler, power Doppler provides greater detail about blood flow and is particularly useful for analyzing vessels at greater depths and with low-velocity flow. However, power Doppler does not provide information on the directionality of blood flow. 3D power Doppler represents a more reliable and reproducible approach for the assessment of tumor vasculature [289]. Donnelly *et al.* demonstrated that power Doppler US imaging could be used to assess quantitatively changes in tumor vascularity and blood flow after treatment with radiation and/or a molecular therapeutic (Donnelly et al Radiology 2001). More recently, ultrafast Doppler tomography was used for quantitative assessment of tumor angiogenesis at different stages of cancer development [290]. Another group employed 3D power Doppler aided with Virtual Organ Computer-aided Analysis to characterize flow in tumor blood vessels and to determine the diagnostic threshold for accurate assessment of tumor and therapeutic measures [291]. The quantification and real time information on blood flow along with vessel structural details can provide crucial information to determine the normalization window for optimal cancer treatment.

Originally, ultrasound scatter from red blood cells was used to calculate the Doppler shift. However, red blood cells are poor scatterers, which made estimating flow velocities in deep-seated vessels with Doppler ultrasound challenging. Ultrasound contrast agents (UCA) can be used to overcome this shortcoming and enable characterization of hemodynamics in tumor vasculature with Doppler US imaging. Krix *et al.* demonstrated that contrast-enhanced power Doppler US imaging could be used to monitor changes in blood volume and mean flow velocity in tumors during growth and during anti-VEGF2 treatment [292]. Unfortunately, Doppler US imaging operated at clinical frequencies (<10 MHz) cannot resolve flow in vessels smaller than a few hundred microns, which are typically the first to respond to antiangiogenic agents. This shortcoming can be addressed with high-frequency ultrasound transducers, thus enabling characterization of blood flow in

small vessels in solid tumors with Doppler US imaging [293–295]. Jugold *et al.* demonstrated that three dimensional 30-MHz Doppler ultrasound could be used to assess the response of tumor vessels with small diameters to anti-angiogenic therapy in murine tumor xenografts [296]. However, the imaging depth of high-frequency ultrasound is severely limited due to acoustic attenuation. To address this limitation, researchers are developing novel signal processing schemes for super resolution ultrasound imaging without sacrificing imaging depth, as described in the following section.

Another limitation of clinical Doppler is low sensitivity to slow blood flow, which may occur during anti-angiogenetic therapy. To address this challenge, Ultrasound microvessel imaging (UMI) has been developed. UMI employs high frame rate plane wave imaging and Eigen base clutter filters to improve the signal-to-noise ratio in Doppler sonography, thus improve the ability to analyze slow-velocity blood flow [297, 298].

Super-resolution US imaging

One of the inherent limitations of conventional diagnostic US modalities is the inability to image the microvasculature due to acoustic diffraction-limited spatial resolution. To evaluate and monitor vascular response to treatment, the ability to visualize and investigate both structural and functional aspects of microvasculature is critically important. This has fueled the development of super resolution US imaging. Super-resolution US imaging is based on centroid localization and tracking of individual microbubbles, which enables sub-diffraction US imaging at depths up to a few centimeters [299]. Christen *et. al* reported super-resolved images and velocity maps from an unmodified clinical US system utilizing postprocessing localization algorithms [299]. They were able to resolve vessels in US images with a diameter of 10 μm at imaging depths exceeding 1 cm. Researchers have demonstrated that super resolution US imaging can visualize structural changes in tumor microvasculature in response to bevacizumab [300]. Additional studies are needed to assess the correlation between changes in microvasculature detected with SR US imaging and tumor response to treatment.

Two major factors that limit the resolution for resolving microvasculature are localization uncertainties and localization densities. Moreover, the ultrasound contrast agent concentration is kept low in order to localize and track individual microbubbles. The scattered ultrasound signal from individual microbubbles is relatively weak, but this can be overcome by acquiring and combining thousands of images of circulating microbubbles. Unfortunately, the time required to acquire and process thousands of images to achieve a sufficient signal-to-noise ratio makes super resolution image construction in real time extremely difficult. Researchers are exploring various approaches for reducing the number of images or the time required for processing in order to make real-time SR ultrasound imaging achievable [301–303]. Super resolution US would undoubtedly advance diagnostic capability of US to a next level. However, super resolution US is still in its nascent stage limited by physical and computational attributes.

Photoacoustic imaging

Photoacoustic imaging (PAI) also known as optoacoustic imaging is a hybrid technology that integrates optical and acoustic aspects of imaging technology to enable higher spatial resolution at greater imaging depth. Optical imaging such as a confocal microscope, multi-photon microscope, and optical coherence tomography provided superior spatial resolution; however, the imaging depth is limited to a few millimeters in highly scattering tissues and therefore can be restricted to the assessment of superficial vasculature. On the other hand, ultrasound imaging, though limited in spatial resolution, provides greater imaging depth. PAI has emerged as a promising modality to address the traditional limitation of both optical and acoustic imaging. It is a non-ionizing, safe and noninvasive imaging approach and therefore has gained rapid momentum in clinical diagnostic imaging [304]. Photoacoustic imaging leverages the acoustic component to overcome the fundamental penetration limit of optical imaging. The photoacoustic effect is the physical phenomenon describing the generation of acoustic waves following laser irradiation and photon absorption. When biological tissues are irradiated with a laser, the photons are absorbed and converted into heat resulting in thermoelastic expansion of tissues. The resulting transient thermal expansion of tissue generates acoustic waves proportional to the optical absorption of endogenous chromophores such as hemoglobin, lipid, and melanin. These acoustic waves are detected by a transducer and are processed to generate images. The endogenous chromophores, hemoglobin in particular, interest the scientific community at large as they enable visualization and characterization of vasculature without utilizing additional contrast agents. Additionally, photoacoustic imaging of hemoglobin can be used to quantify oxygen saturation in blood vessels.

As such, PA imaging can serve as a non-invasive label-free approach for the assessment of microvasculature through various structural or geometric parameters such as vessel diameter, density, tortuosity, and fractal dimensions [305]. These attributes of PA imaging make it an attractive alternative to determine, evaluate and monitor vascular normalization following antiangiogenic

therapies or other therapeutic measures. The major modalities of photoacoustic imaging used in the assessment of vasculature include Photoacoustic Microscopy, Photoacoustic Tomography, and Photoacoustic endoscopy/Intravital imaging. Photoacoustic endoscopy is primarily used to visualize lipid deposits in atherosclerotic plaques in arteries. Photoacoustic endoscopy is beyond the scope of this article and therefore will not be discussed.

Photoacoustic microscopy (PAM)

Photoacoustic microscopy, similar to optical microscopy systems, provides a high spatial resolution of 1-2 μm at a comparable imaging depth of 0.2-1 mm. The extinction coefficient for oxyhemoglobin (HbO_2) and deoxyhemoglobin (Hb) varies with wavelength, and PAI systems leverage these differing spectral characteristics to estimate oxygen saturation in blood vessels and the surrounding tissue through spectral unmixing algorithms [306]. PAM has been used to resolve structural and functional features of vasculature, such as morphology, oxygen saturation, and blood flow in the brain with an intact skull [307] or through a cranial window. PAM can be classified into (i) optical-resolution photoacoustic microscopy (OR-PAM), and (ii) acoustic resolution photoacoustic microscopy (AR-PAM).

OR-PAM

OR-PAM has been successfully used to resolve structural, functional, molecular, and genetic characteristics at the cellular and subcellular level through both endogenous and exogenous contrast agents [308]. OR-PAM uses a highly focused laser beam for excitation and a focused or unfocused ultrasound transducer for detection of acoustic emissions. OR-PAM is performed by point scanning the overlapping foci of the transmitting laser and the receiving ultrasound transducer. The optical focal spot size of the focused laser determines the lateral resolution whereas axial resolution is determined by the transducer's bandwidth. The optoacoustic beam combiner technology is commonly used for *in vivo* microvascular imaging to tightly focus light providing a lateral resolution below 5 μm at an imaging depth on the order of a millimeter [309, 310]. The lateral resolution, however, can be reduced at the expense of imaging depth [308]. Various design and computational strategies are being pursued to improve sensitivity and imaging depth, [311–314] and for preclinical imaging [315]. For instance, OR-PAM has been used to evaluate hemodynamics in the brain of anesthetized [316] or awake mice [307, 317].

Zhou *et. al* recently monitored longitudinal vascular changes and identified a normalization window in a mouse ear prostate cancer xenograft following anti-angiogenic therapy [318]. The vessel diameter, density, and tortuosity were successfully quantified in OR-PAM images to assess tumor development. Following treatment with DC101, a significant decrease in vessel diameter and tortuosity was observed whereas the overall vessel density remained unaffected. These observations were further validated with histological analysis. It was also shown that the normalized vasculature gave rise to an increased accumulation and homogeneous distribution of the chemotherapeutic agent in the tumor. They reported gradual vascular normalization until day 5 following DC101 treatment, after which the normalized vessels were eliminated. Another study demonstrated the feasibility of OR-PAM in the diagnosis of ovarian cancer [319]. They reported differences in vessel volume, length, and the number of segments in benign vs malignant excised ovarian and fallopian tube specimens. Although they were able to distinguish malignancy in the excised ovary, adopting this approach for *in vivo* assessment would prove challenging due to the limited imaging depth of OR-PAM.

AR-PAM

Unlike OR-PAM, AR-PAM utilizes a lightly focused laser beam for illumination and a focused transducer for detection. Similar to OR-PAM, the axial resolution of AR-PAM is determined by the transducer's bandwidth. However, the lateral resolution is determined by the central frequency and numerical aperture of the transducer [320]. In AR-PAM, both lateral resolution and imaging depth can be tuned based on the frequency of the transducers [321]. For instance, a higher frequency transducer provides better lateral resolution but with limited imaging depth due to higher acoustic attenuation in biological tissue. A lateral resolution of 45 μm and an imaging depth of 3mm have been reported with a 50 MHz transducer. On the other hand, lower frequency transducers can be utilized for imaging at deeper locations but with lateral resolution trade-offs [320, 322].

Real-time PAM imaging, however, has been hindered by slow scanning speeds of the laser focus [307]. The implementation of different scanning technology such as MEMS scanners, and voice coils have improved PAM imaging [323]. Wang *et. al* demonstrated real-time imaging of single-flowing red blood cells delivering oxygen with a temporal resolution of milliseconds [324]. Although, very powerful, PAM might be limited in its ability to investigate structural and functional aspects of vasculature to accurately determine normalized window or vascular response to therapy in deep seated cancers.

Photoacoustic mesoscopy and macroscopy

Unlike PAM, which has limited imaging depth, Photoacoustic mesoscopy and maroscopy enable deep tissue imaging [282]. Mesoscopy can be described as a bridge between PAM and PA macroscopy [325]. Mesoscopy refers to imaging depth up to 5mm with the resolution ranging from few microns to tens of microns, whereas macroscopy refers to the imaging depth beyond 5mm with depth dependent resolution ranging from tens of micros to a few hundred microns [282]. The imaging performance of these classes of photoacoustic imaging relies on ultrasound sensors and dectectors geometry as well as image receonstruction algorithms.

Photoacoustic mesoscopy

Photoacoustic mesoscopy or raster scanning optoacoustic mesoscopy (RSOM) is a modified concept of AR-PAM that utilizes wide-field optical illumination and single tightly focused high center frequency transducers [326]. RSOM provides superior resolution, in the range of 15 – 40 μm with the imaging depth of 2 mm, enough to distinguish vessels of different sizes and resolve vascular response to cancer therapy [327]. For example, Raster-scanning optoacoustic angiography was used to characterize and quantify neoangiogenesis in colon cancer models [328]. In one study, RSOM was able to image vessels with 20 μm diameter as well as identified the small changes within the vascular network of tumor [329].

Photoacoustic tomography

Photoacoustic tomography (PAT) is the traditional form of PAI macroscopy that has been extensively investigated for qualitative and quantitative imaging and evaluation of deeper vasculature. Similar to PAM, PAT capitalizes on the strong absorbance of hemoglobin to image the blood vessel network and does not require additional exogenous contrast agents. This capability of PAT has opened up multiple avenues for diagnostic research, particularly in diseases such as cancer and cardiovascular disease, which are characterized by significant changes in functional and morphological aspects of the vasculature at increasing depth. As such, one of the primary applications of PAT is detecting and monitoring vasculature changes during disease progression and assessing the role of the vasculature in disease development. For example, Lao *et. al* investigated the morphological changes in tumor vasculature over 20 days following the subcutaneous inoculation of breast cancer tumor cells in a small animal model [330]. PAT also can be used as an imaging tool for evaluating the therapeutic efficacy of a treatment regimen. PAT has been used to monitor transient vascular normalization and to determine the optimal window for delivering cancer therapeutics. In another study, PAT was used to assess the functional measurement of ovarian tumor response to trebananib. PAT demonstrated both vessel regression and normalized vessels following anti-angiogenic treatment which was further validated by serum biomarker profiling of angiopoietin 1 [331]. Besides hemoglobin, other intrinsic absorbers such as melanin and lipids have been explored for the diagnosis of various diseases including melanoma and atherosclerosis respectively.

Multispectral optoacoustic tomography (MSOT) has further expanded the application of photoacoustic imaging, particularly in the functional assessment of vasculature. In addition to resolving blood vessels as small as 100 μm at depths approaching 1 cm, MSOT can assess blood oxygen saturation levels [332]. In MSOT, tissues are illuminated at multiple wavelengths and absorbance spectra are collected. A spectral unmixing algorithm is then used to resolve oxygenated and deoxygenated hemoglobin as an individual absorber and hence differentiate arteries from veins. Oxygen saturation provides perfusion hemodynamics that is crucial to identifying or monitoring a diseased state [333]. For example, low oxygenation (hypoxia) may indicate a tumor [334] or a lower degree of oxygen saturation may indicate vascular diseases.

Various customized and commercial PAT systems built using a wide array of detectors are being continuously designed for improving different aspects of vascular imaging in a variety of research and clinical applications. For instance, Taruttis *et. al* investigated a handheld probe with a concave array for clinical assessment of major blood vessels and microvasculature [332]. In another study, Matsumoto used a hemispherical detector array for 3D imaging of human palmar vessels [335]. An alternative light source such as a light-emitting diode has been explored for point-of-care PAT imaging [336]. Other commercial systems are available for vascular imaging in a selected ROI [337] or whole-body imaging of small animals [338, 339]. Although PA imaging provides better spatial resolution at greater imaging depth, whole-body photoacoustic imaging currently is only applicable to small animal models. The clinical application of PA imaging, though extensively investigated, remains limited to relatively superficial areas of the body unless conducted intraoperatively. Moreover, the utility of PAT in human brain vasculature imaging is severely limited mainly due to a lack of sensitivity to functional changes, imaging speed, penetration depth, and skull-induced aberrations [340]. Nevertheless, continuous efforts are being pursued on instrumentation as well as technical aspects to improve upon existing PA imaging systems for functional imaging of the brain [340–342] and other clinical and preclinical applications [343, 344].

While significant advancements in commercial PAT systems have been achieved, most vasculature imaging continues to be performed using a customized system. Therefore, PAT still lacks a standardized protocol for the clinical evaluation of images generated by these systems, but initiatives have been started at multiple levels to establish PAT as a standardized clinical imaging tool in the near future [345].

Histopathology and immunohistochemistry for validation

Histopathology and immunohistochemistry are the "gold standards" for the evaluation of biological and molecular changes associated with disease pathology or therapeutic response. Regardless of the imaging technology being used for qualitative or quantitative assessment of structural or functional changes associated with vascular response to therapy, it is almost always validated using histology or immunohistochemistry in the research setting. For example, chenages in microvessel density can be examined via immunohistochemistry [346]. This method uses labeled antibodies that bind with biomarkers of the endothelium such as CD31, CD105, and CD34, followed by counting the microvessels under high magnification at a predefined number of hot spots or randomly selected microscopic fields. In a clinical setting, angiogenesis is graded through subjective scoring to determine the correlation with tumor parameters such as malignancy, size, or cancer type [347].

Similar methods can be utilized to examine the morphology of blood vessels in solid tumors. Specific markers for smooth muscle cells and/or pericytes are used to differentiate tumor vasculature from normalized vasculature following anti-angiogenic therapies. α-SMA (smooth muscle actin) is the most common marker used to evaluate vascular morphology. Some other markers such as SM22α [348] have also been used. Common markers for pericytes include α-SMA, high molecular weight melanoma-associated antigen (NG2), desmin, and PDGFR-β. The colocalization of both smooth muscle and pericyte markers in immunohistochemical slides may also be used in the morphological assessment of normalized vasculature [349]. For example, a ratio of pericyte-to-endothelial cells (α-SMA/CD31) can provide information on vessel maturity [19].

Although immunohistochemistry is widely used as a validation technique in a research setting, the lack of a standardized process, a wide range of antibodies used from various suppliers, and differences in manual labeling and counting procedures may introduce significant variations in results from separate research groups. Additionally, histology and immunohistochemistry are performed as an endpoint experiment, which limits their usefulness for monitoring vascular response to treatment regimen. Histological analysis is mostly used as a qualitative measure, and its use as a quantitative analysis is user-dependent and prone to variations among users due to a lack of standardized procedure. Most imaging technology focuses on providing information similar to histological analysis but with minimal invasiveness and in a relatively short time.

Conclusion and future outlook

In this review, we discussed the different imaging modalities used for characterizing and monitoring vascular changes following cancer onset or anti-angiogenic therapy. The structural and functional changes in vasculature provide crucial insights into cancer disease development as well as therapeutic outcomes. In anti-angiogenic therapy, this information can provide an optimal window for drug delivery to maximize the therapeutic effect. All the imaging techniques presented here have been used for vascular imaging in some capacity, and each modality has its positive and negatives. MRI, CT, and PET can be used for vascular imaging throughout the entire body at the expense of spatial and temporal resolution. Optical and ultrasound imaging modalities are capable of imaging microvasculature at the expense of imaging depth and field of view. Each modality has its own collection of contrast agents that can be used to extend imaging depth, allow for detection of smaller vasculature, or to enable analysis of hemodynamic properties. Moreover, innovative approaches to data acquisition and processing has enabled most imaging modalities to characterize vascular physiology and function, including perfusion, vascular permeability, and blood oxygenation levels. Photoacoustic imaging is an emerging imaging modality capable of evaluating blood oxygen levels without the use of exogenous contrast agents. Multiple imaging modalities also may be combined to overcome respective limitations and to assess the structure and function of blood vessels across multiple scales. There are several treatment strategies capable of altering the morphology and the performance of blood vessels, including radiation and anti-angiogenic drugs. The ability to monitor vascular response longitudinally provides clinicians with the information needed to adjust treatment parameters and maximize therapeutic efficacy. Moreover, imaging the vascular response may be key to identifying the vascular normalization window and exploring new and effective combinations of anti-angiogenic agents and anticancer drugs.

Anti-vascular agents such as bevacizumab, sunitinib, ramucirumab, sorafenib, regorafenib, etc are usually used in combination with chemotherapeutics or immunotherapeutics to improve patient outcomes. Employing

one or a combination of the discussed imaging modalities to optimize dosing, identify the optimal delivery window, and determine the sequence of drug administration to maximize the therapeutic benefits would be ideal. However, despite the diagnostic potential of these imaging modalities in vascular assessment, they have yet to be integrated into standard clinical practice to attain such goals. The ultimate challenge in achieving these goals are (i) differences in tumor progression and therapeutic response in animal and human tumors, (ii) inter- and intra-spatial and temporal heterogeneity in tumors resulting in variable therapeutic response within the tumor, and (iii) variable timing and extent of normalization window. More preclinical work to optimize combination regimes, novel biomarkers for identifying normalization phenotype, and better contrast agents, in part, may address the current challenges in the field. Nonetheless, vascular imaging will likely continue to develop as an impactful technique for the diagnosis and treatment of cancer.

Acknowledgements
Not applicable.

Authors' contributions
All authors contributed to the preparation of this manuscript.

Funding
The authors thank the National Institute of Biomedical Imaging and Bioengineering for partial financial support.

Availability of data and materials
Not applicable.

Declarations

Ethics approval and consent to participate
Not applicable.

Consent for publication
Not applicable.

Competing interests
The authors declare no conflict of interest.

Received: 16 January 2024 Accepted: 26 August 2024
Published online: 23 October 2024

References

1. Kim KJ, Li B, Winer J, Armanini M, Gillett N, Phillips HS, Ferrara N. Inhibition of vascular endothelial growth factor-induced angiogenesis suppresses tumour growth in vivo. Nature. 1993;362(6423):841–4.
2. Jain RK, Duda DG, Clark JW, Loeffler JS. Lessons from phase III clinical trials on anti-VEGF therapy for cancer. Nat Clin Pract Oncol. 2006;3(1):24–40.
3. Sandler A, Gray R, Perry MC, Brahmer J, Schiller JH, Dowlati A, Lilenbaum R. Johnson DHJNEJoM: Paclitaxel–carboplatin alone or with bevacizumab for non–small-cell lung cancer. N Engl J Med. 2006;355(24):2542–50.
4. Reck M, Von Pawel J. Zatloukal Pv, Ramlau R, Gorbounova V, Hirsh V, Leighl N, Mezger J, Archer V, Moore NJAoo: Overall survival with cisplatin–gemcitabine and bevacizumab or placebo as first-line therapy for nonsquamous non-small-cell lung cancer: results from a randomised phase III trial (AVAiL). Ann Oncol. 2010;21(9):1804–9.
5. Tong RT, Boucher Y, Kozin SV, Winkler F, Hicklin DJ. Jain RKJCr: Vascular normalization by vascular endothelial growth factor receptor 2 blockade induces a pressure gradient across the vasculature and improves drug penetration in tumors. Cancer Res. 2004;64(11):3731–6.
6. Hurwitz H, Fehrenbacher L, Novotny W, Cartwright T, Hainsworth J, Heim W, Berlin J, Baron A. Bevacizumab plus irinotecan, fluorouracil, and leucovorin for metastatic colorectal cancer. N Engl J Me. 2004;350(23):2335–42.
7. Huang Y, Yuan J, Righi E, Kamoun WS, Ancukiewicz M, Nezivar J, Santosuosso M, Martin JD, Martin MR, Vianello F. Vascular normalizing doses of antiangiogenic treatment reprogram the immunosuppressive tumor microenvironment and enhance immunotherapy. Proc Natl Acad Sci. 2012;109(43):17561–6.
8. Goel S, Duda DG, Xu L, Munn LL, Boucher Y, Fukumura D, Jain RK. Normalization of the vasculature for treatment of cancer and other diseases. Physiol Rev. 2011;91(3):1071–121.
9. Duda DG. Molecular biomarkers of response to antiangiogenic therapy for cancer. Int Sch Res Not. 2012;2012(1):587259.
10. Fukumura D, Duda DG, Munn LL, Jain RK. Tumor microvasculature and microenvironment: novel insights through intravital imaging in preclinical models. Microcirculation. 2010;17(3):206–25.
11. Wang S, Liu J, Goh CC, Ng LG, Liu B. NIR-II-Excited Intravital Two-Photon Microscopy Distinguishes Deep Cerebral and Tumor Vasculatures with an Ultrabright NIR-I AIE Luminogen. Adv Mater. 2019;31(44): e1904447.
12. Kalpathy-Cramer J, Gerstner ER, Emblem KE, Andronesi O, Rosen B. Advanced magnetic resonance imaging of the physical processes in human glioblastoma. Cancer Res. 2014;74(17):4622–37.
13. Kickingereder P, Sahm F, Wiestler B, Roethke M, Heiland S, Schlemmer H-P, Wick W, von Deimling A, Bendszus M, Radbruch A. Evaluation of microvascular permeability with dynamic contrast-enhanced MRI for the differentiation of primary CNS lymphoma and glioblastoma: radiologic-pathologic correlation. Am J Neuroradiol. 2014;35(8):1503–8.
14. Padhani AR, Khan AA. Diffusion-weighted (DW) and dynamic contrast-enhanced (DCE) magnetic resonance imaging (MRI) for monitoring anticancer therapy. Target Oncol. 2010;5(1):39–52.
15. Agrawal R, Li LKH, Nakhate V, Khandelwal N, Mahendradas P. Choroidal vascularity index in Vogt-Koyanagi-Harada disease: an EDI-OCT derived tool for monitoring disease progression. Translational vision science & technology. 2016;5(4):7–7.
16. Clark DP, Ghaghada K, Moding EJ, Kirsch DG, Badea CT. In vivo characterization of tumor vasculature using iodine and gold nanoparticles and dual energy micro-CT. Phys Med Biol. 2013;58(6):1683.
17. Cui Y, Liu H, Liang S, Zhang C, Cheng W, Hai W, Yin B, Wang D. The feasibility of 18F-AlF-NOTA-PRGD2 PET/CT for monitoring early response of Endostar antiangiogenic therapy in human nasopharyngeal carcinoma xenograft model compared with 18F-FDG. Oncotarget. 2016;7(19):27243.
18. Valable S, Petit E, Roussel S, Marteau L, Toutain J, Divoux D, Sobrio F, Delamare J, Barre L, Bernaudin M. Complementary information from magnetic resonance imaging and (18)F-fluoromisonidazole positron emission tomography in the assessment of the response to an antiangiogenic treatment in a rat brain tumor model. Nucl Med Biol. 2011;38(6):781–93.
19. Ho YJ, Chu SW, Liao EC, Fan CH, Chan HL, Wei KC, Yeh CK. Normalization of Tumor Vasculature by Oxygen Microbubbles with Ultrasound. Theranostics. 2019;9(24):7370–83.
20. Ahn J, Kim JY, Choi W, Kim C. High-resolution functional photoacoustic monitoring of vascular dynamics in human fingers. Photoacoustics. 2021;23: 100282.
21. Bench C, Hauptmann A, Cox BT. Toward accurate quantitative photoacoustic imaging: learning vascular blood oxygen saturation in three dimensions. J Biomed Opt. 2020;25(8): 085003.
22. Bi R, Balasundaram G, Dinish U, Jeon S, Imai T, Pu Y, Ng LG, Kim C, Wan L, Olivo M. Functional vascular imaging by Photoacoustic Microscopy (PAM) and its biomedical application. In: Optical Biopsy XVII: Toward

Real-Time Spectroscopic Imaging and Diagnosis: 2019: International Society for Optics and Photonics. 2019. p. 108730B.
23. Jain RK. Normalization of tumor vasculature: an emerging concept in antiangiogenic therapy. Science. 2005;307(5706):58–62.
24. Guo Y, et al. High-resolution whole-brain DCE-MRI using constrained reconstruction: Prospective clinical evaluation in brain tumor patients. Med Phys. 2016;43:2013.
25. Yankeelov TE, Gore JC. Dynamic Contrast Enhanced Magnetic Resonance Imaging in Oncology: Theory, Data Acquisition, Analysis, and Examples. Curr Med Imaging Rev. 2009;3:91–107.
26. Lim WH, Park JS, Park J, Choi SH. Assessing the reproducibility of high temporal and spatial resolution dynamic contrast-enhanced magnetic resonance imaging in patients with gliomas. Sci Rep. 2021;11:23217.
27. Chakhoyan A, Leu K, Pope WB, Cloughesy TF, Ellingson BM. Improved Spatiotemporal Resolution of Dynamic Susceptibility Contrast Perfusion MRI in Brain Tumors Using Simultaneous Multi-Slice Echo-Planar Imaging. AJNR Am J Neuroradiol. 2018;39:43–5.
28. Quarles CC, Bell LC, Stokes AM. Imaging vascular and hemodynamic features of the brain using dynamic susceptibility contrast and dynamic contrast enhanced MRI. Neuroimage. 2019;187:32–55.
29. Skinner JT, Moots PL, Ayers GD, Quarles CC. On the Use of DSC-MRI for Measuring Vascular Permeability. Am J Neuroradiol. 2016;37:80–7.
30. García-Figueiras R, et al. CT Perfusion in Oncologic Imaging: A Useful Tool? Am J Roentgenol. 2013;200:8–19.
31. Jain R. Perfusion CT Imaging of Brain Tumors: An Overview. Am J Neuroradiol. 2011;32:1570–7.
32. Jain R, et al. Quantitative Estimation of Permeability Surface-Area Product in Astroglial Brain Tumors Using Perfusion CT and Correlation with Histopathologic Grade. AJNR Am J Neuroradiol. 2008;29:694–700.
33. Tachiiri T, et al. Vascular Normalization Caused by Short-Term Lenvatinib Could Enhance Transarterial Chemoembolization in Hepatocellular Carcinoma. Curr Oncol. 2023;30:4779–86.
34. Machida H, et al. Dual-Energy Spectral CT: Various Clinical Vascular Applications. Radiographics. 2016;36:1215–32.
35. Alizzi Z, Gogbashian A, Karteris E, Hall M. Development of a dual energy CT based model to assess response to treatment in patients with high grade serous ovarian cancer: a pilot cohort study. Cancer Imaging. 2023;23:62.
36. Zegadło A, Różyk A, Żabicka M, Więsik-Szewczyk E, Maliborski A. Dual-energy computed tomography as a lower radiation dose alternative to perfusion computed tomography in tumor viability assessment. Sci Rep. 2023;13:120.
37. Dewaguet J, et al. Dual-Energy CT Perfusion of Invasive Tumor Front in Non-Small Cell Lung Cancers. Radiology. 2022;302:448–56.
38. Mirus M, et al. Noninvasive assessment and quantification of tumor vascularization using [18F]FDG-PET/CT and CE-CT in a tumor model with modifiable angiogenesis—an animal experimental prospective cohort study. EJNMMI Res. 2019;9:55.
39. Vaquero JJ, Kinahan P. Positron Emission Tomography: Current Challenges and Opportunities for Technological Advances in Clinical and Preclinical Imaging Systems. Annu Rev Biomed Eng. 2015;17:385–414.
40. Watakabe T, et al. High Spatial Resolution Digital Positron Emission Tomography Images With Dedicated Source-to-background Algorithm for Radiotherapy Planning. Anticancer Res. 2020;40:2567–72.
41. Kristian A, et al. Dynamic 18F-FDG-PET for monitoring treatment effect following anti-angiogenic therapy in triple-negative breast cancer xenografts. Acta Oncol. 2013;52:1566–72.
42. Moses WW. Fundamental Limits of Spatial Resolution in PET. Nucl Instrum Methods Phys Res A. 2011;648 Supplement 1:S236–40.
43. Popescu DP, et al. Optical coherence tomography: fundamental principles, instrumental designs and biomedical applications. Biophys Rev. 2011;3:155.
44. Greig EC, Duker JS, Waheed NK. A practical guide to optical coherence tomography angiography interpretation. Int J Retina Vitr. 2020;6:55.
45. Gao SS, et al. Optical Coherence Tomography Angiography. Invest Ophthalmol Vis Sci. 2016;57(9):OCT27–36.
46. Hielscher AH, et al. Near-infrared diffuse optical tomography. *Dis*. Markers. 2002;18:313–37.
47. Doulgerakis M, Eggebrecht AT, Dehghani H. High-density functional diffuse optical tomography based on frequency-domain measurements improves image quality and spatial resolution. Neurophotonics. 2019;6:035007.
48. Carp, S. A. & Fang, Q. Diffuse Optical Imaging. in Pathobiology of Human Disease (eds. McManus, L. M. & Mitchell, R. N.) 3925–3942 (Academic Press, 2014). https://doi.org/10.1016/B978-0-12-386456-7.07605-X.
49. Paull PE, Hyatt BJ, Wassef W, Fischer AH. Confocal laser endomicroscopy: a primer for pathologists. Arch Pathol Lab Med. 2011;135:1343–8.
50. Wang J, et al. A Confocal Endoscope for Cellular Imaging. Engineering. 2015;1:351–60.
51. De Palma GD, et al. In vivo assessment of tumour angiogenesis in colorectal cancer: the role of confocal laser endomicroscopy. Colorectal Dis. 2016;18:O66–73.
52. Liu H, et al. Confocal endomicroscopy for in vivo detection of microvascular architecture in normal and malignant lesions of upper gastrointestinal tract. J Gastroenterol Hepatol. 2008;23:56–61.
53. Pilonis ND, Januszewicz W, di Pietro M. Confocal laser endomicroscopy in gastro-intestinal endoscopy: technical aspects and clinical applications. Transl Gastroenterol Hepatol. 2022;7:7.
54. Mehta KS, Lee JJ, Taha AG, Avgerinos E, Chaer RA. Vascular applications of contrast-enhanced ultrasound imaging. J Vasc Surg. 2017;66:266–74.
55. Ho Y-J, et al. Normalization of Tumor Vasculature by Oxygen Microbubbles with Ultrasound. Theranostics. 2019;9:7370–83.
56. Shelton SE, Stone J, Gao F, Zeng D, Dayton PA. Microvascular Ultrasonic Imaging of Angiogenesis Identifies Tumors in a Murine Spontaneous Breast Cancer Model. Int J Biomed Imaging. 2020;2020:7862089.
57. Dietrich CF, et al. How to perform Contrast-Enhanced Ultrasound (CEUS). Ultrasound Int Open. 2018;4:E2–15.
58. Leen E, et al. Dynamic contrast enhanced ultrasound assessment of the vascular effects of novel therapeutics in early stage trials. Eur Radiol. 2012;22:1442–50.
59. Demi L, Van Sloun RJG, Wijkstra H, Mischi M. Towards Dynamic Contrast Specific Ultrasound Tomography. Sci Rep. 2016;6:34458.
60. Gao R, et al. Achieving depth-independent lateral resolution in AR-PAM using the synthetic-aperture focusing technique. Photoacoustics. 2022;26: 100328.
61. Moothanchery M, et al. High-speed simultaneous multiscale photoacoustic microscopy. J Biomed Opt. 2019;24: 086001.
62. Moothanchery M, et al. Optical resolution photoacoustic microscopy based on multimode fibers. Biomed Opt Express. 2018;9(3):1190–7.
63. Steinberg I, et al. Photoacoustic clinical imaging Photoacoustics. 2019;14:77–98.
64. Zhou Y, Yao J, Wang LV. Tutorial on photoacoustic tomography. J Biomed Opt. 2016;21: 061007.
65. Zhang J, Duan F, Liu Y, Nie L. High-Resolution Photoacoustic Tomography for Early-Stage Cancer Detection and Its Clinical Translation. Radiol Imaging Cancer. 2020;2: e190030.
66. Xia J, et al. Whole-body ring-shaped confocal photoacoustic computed tomography of small animals in vivo. J Biomed Opt. 2012;17: 050506.
67. Hartung MP, Grist TM, François CJ. Magnetic resonance angiography: current status and future directions. J Cardiovasc Magn Reson. 2011;13(1):19.
68. Englund EK, Langham MC. Quantitative and Dynamic MRI Measures of Peripheral Vascular Function. Front Physiol. 2020;11:120.
69. Murphy DJ, Aghayev A, Steigner ML. Vascular CT and MRI: a practical guide to imaging protocols. Insights Imaging. 2018;9(2):215–36.
70. Gordon Y, Partovi S, Müller-Eschner M, Amarteifio E, Bäuerle T, Weber M-A, Kauczor H-U, Rengier F. Dynamic contrast-enhanced magnetic resonance imaging: fundamentals and application to the evaluation of the peripheral perfusion. Cardiovasc Diagn Ther. 2014;4(2):147.
71. Wu L, Lv P, Zhang H, Fu C, Yao X, Wang C, Zeng M, Li Y. Wang XJMRI: Dynamic contrast-enhanced (DCE) MRI assessment of microvascular characteristics in the murine orthotopic pancreatic cancer model. Magn Reson Imaging. 2015;33(6):737–60.
72. Yan Y, Sun X, Shen B. Contrast agents in dynamic contrast-enhanced magnetic resonance imaging. Oncotarget. 2017;8(26):43491.
73. Lee DH. Mechanisms of contrast enhancement in magnetic resonance imaging. Can Assoc Radiol J. 1991;42(1):6–12.
74. Tofts PS. Modeling tracer kinetics in dynamic Gd-DTPA MR imaging. J Magn Reson Imaging. 1997;7(1):91–101.

75. Tofts PS, Brix G, Buckley DL, Evelhoch JL, Henderson E, Knopp MV, Larsson HB, Lee TY, Mayr NA, Parker GJ, Taylor J, Weisskoff RM. Estimating kinetic parameters from dynamic contrast-enhanced T1-weighted MRI of a diffusable tracer: standardized quantities and symbols. J Magn Reson Imaging. 1999;10(3):223–32.
76. Nielsen T, Wittenborn T, Horsman MR. Dynamic Contrast-Enhanced Magnetic Resonance Imaging (DCE-MRI) in Preclinical Studies of Antivascular Treatments. Pharmaceutics. 2012;4(4):563–89.
77. Yankeelov TE, Gore JC. Dynamic Contrast Enhanced Magnetic Resonance Imaging in Oncology: Theory, Data Acquisition, Analysis, and Examples. Current Medical Imaging Reviews. 2009;3(2):91–107.
78. Kalpathy-Cramer J, Gerstner ER, Emblem KE, Andronesi OC, Rosen B. Advanced magnetic resonance imaging of the physical processes in human glioblastoma. Cancer Res. 2014;74(17):4622–37.
79. Zhang J, Liu H, Tong H, Wang S, Yang Y, Liu G, Zhang W. Clinical applications of contrast-enhanced perfusion MRI techniques in gliomas: recent advances and current challenges. Contrast Media Mol Imaging. 2017;2017:7064120.
80. Gordon Y, Partovi S, Müller-Eschner M, Amarteifio E, Bäuerle T, Weber M-A, Kauczor H-U, Rengier F. Dynamic contrast-enhanced magnetic resonance imaging: fundamentals and application to the evaluation of the peripheral perfusion. Cardiovas Diagn Ther. 2014;4(2):147.
81. Shao J, Zhang Z, Liu H, Song Y, Yan Z, Wang X, Hou Z. DCE-MRI pharmacokinetic parameter maps for cervical carcinoma prediction. Comput Biol Med. 2020;118: 103634.
82. Nagasaka K, Satake H, Ishigaki S, Kawai H, Naganawa S. Histogram analysis of quantitative pharmacokinetic parameters on DCE-MRI: correlations with prognostic factors and molecular subtypes in breast cancer. Breast Cancer. 2019;26(1):113–24.
83. Ahmed Z, Levesque IR. Pharmacokinetic modeling of dynamic contrast-enhanced MRI using a reference region and input function tail. Magn Reson Med. 2020;83(1):286–98.
84. Lecler A, Balvay D, Cuenod C-A, Marais L, Zmuda M, Sadik J-C, Galatoire O, Farah E, El Methni J, Zuber K, et al. Quality-based pharmacokinetic model selection on DCE-MRI for characterizing orbital lesions. J Magn Reson Imaging. 2019;50(5):1514–25.
85. Crombé A, Saut O, Guigui J, Italiano A, Buy X, Kind M. Influence of temporal parameters of DCE-MRI on the quantification of heterogeneity in tumor vascularization. J Magn Reson Imaging. 2019;50(6):1773–88.
86. Wu C, Pineda F, Hormuth DA II, Karczmar GS, Yankeelov TE. Quantitative analysis of vascular properties derived from ultrafast DCE-MRI to discriminate malignant and benign breast tumors. Magn Reson Med. 2019;81(3):2147–60.
87. Gaustad J-V, Hauge A, Wegner CS, Simonsen TG, Lund KV, Hansem LMK, Rofstad EK. DCE-MRI of Tumor Hypoxia and Hypoxia-Associated Aggressiveness. Cancers. 2020;12(7):1979.
88. Nilsen LB, Fangberget A, Geier OM, Engebraaten O, Borgen E, Olsen DR, Seierstad T. Associations between tumor vascularization assessed by in vivo DCE-MRI and the presence of disseminated tumor cells in bone marrow in breast cancer patients at the time of diagnosis. J Magn Reson Imaging. 2014;40(6):1382–91.
89. Barnes SR, Ng TSC, Montagne A, Law M, Zlokovic BV, Jacobs RE. Optimal acquisition and modeling parameters for accurate assessment of low Ktrans blood-brain barrier permeability using dynamic contrast-enhanced MRI. Magn Reson Med. 2016;75(5):1967–77.
90. Dickie BR, Rose CJ, Kershaw LE, Withey SB, Carrington BM, Davidson SE, Hutchison G, West CML. The prognostic value of dynamic contrast-enhanced MRI contrast agent transfer constant Ktrans in cervical cancer is explained by plasma flow rather than vessel permeability. Br J Cancer. 2017;116(11):1436–43.
91. Cuenod CA, Balvay D. Perfusion and vascular permeability: Basic concepts and measurement in DCE-CT and DCE-MRI. Diagn Interv Imaging. 2013;94(12):1187–204.
92. Meyer HJ, Wienke A, Surov A. Correlation Between Ktrans and Microvessel Density in Different Tumors: A Meta-analysis. Anticancer Res. 2018;38(5):2945–50.
93. Kim SH, Lee HS, Kang BJ, Song BJ, Kim H-B, Lee H, Jin M-S, Lee A. Dynamic Contrast-Enhanced MRI Perfusion Parameters as Imaging Biomarkers of Angiogenesis. PLoS ONE. 2016;11(12): e0168632.
94. Yeo D-M, Oh SN, Jung C-K, Lee MA, Oh ST, Rha SE, Jung SE, Byun JY, Gall P, Son Y. Correlation of dynamic contrast-enhanced MRI perfusion parameters with angiogenesis and biologic aggressiveness of rectal cancer: Preliminary results. Journal of magnetic resonance imaging: JMRI. 2015;41(2):474–80.
95. Nagaraja TN, Elmghirbi R, Brown SL, Rey JA, Schultz L, Mukherjee A, Cabral G, Panda S, Lee IY, Sarntinoranont M, et al. Imaging acute effects of bevacizumab on tumor vascular kinetics in a preclinical orthotopic model of U251 glioma. NMR Biomed. 2021;34(7): e4516.
96. Pishko GL, Muldoon LL, Pagel MA, Schwartz DL, Neuwelt EA. Vascular endothelial growth factor blockade alters magnetic resonance imaging biomarkers of vascular function and decreases barrier permeability in a rat model of lung cancer brain metastasis. Fluids and Barriers of the CNS. 2015;12(1):5.
97. Yang J, Liao C, Liu Y, Yang G, Ke T, Ding Y, Li Q. MR imaging biomarkers evaluating vascular normalization window after anti-vessel treatment. Oncotarget. 2018;9(15):11964.
98. Chen BB, Lu YS, Lin CH, Chen WW, Wu PF, Hsu CY, Yu CW, Wei SY, Cheng AL, Shih TT. A pilot study to determine the timing and effect of bevacizumab on vascular normalization of metastatic brain tumors in breast cancer. BMC Cancer. 2016;16:466.
99. Tran A, Koh TS, Prawira A, Ho RZW, Le TBU, Vu TC, Hartano S, Teo XQ, Chen WC, Lee P, et al. Dynamic Contrast-Enhanced Magnetic Resonance Imaging as Imaging Biomarker for Vascular Normalization Effect of Infigratinib in High-FGFR-Expressing Hepatocellular Carcinoma Xenografts. Mol Imag Biol. 2021;23(1):70–83.
100. Sorensen AG, Batchelor TT, Zhang W-T, Chen P-J, Yeo P, Wang M, Jennings D, Wen PY, Lahdenranta J, Ancukiewicz M, et al. A "Vascular Normalization Index" as Potential Mechanistic Biomarker to Predict Survival after a Single Dose of Cediranib in Recurrent Glioblastoma Patients. Can Res. 2009;69(13):5296–300.
101. Kong Z, Yan C, Zhu R, Wang J, Wang Y, Wang Y, Wang R, Feng F, Ma W. Imaging biomarkers guided anti-angiogenic therapy for malignant gliomas. NeuroImage Clin. 2018;20:51–60.
102. Batchelor TT, Gerstner ER, Emblem KE, Duda DG, Kalpathy-Cramer J, Snuderl M, Ancukiewicz M, Polaskova P, Pinho MC, Jennings D, et al. Improved tumor oxygenation and survival in glioblastoma patients who show increased blood perfusion after cediranib and chemoradiation. Proc Natl Acad Sci USA. 2013;110(47):19059–64.
103. Kim Y-E, Joo B, Park M-S, Shin SJ, Ahn JB, Kim M-J. Dynamic Contrast-Enhanced Magnetic Resonance Imaging as a Surrogate Biomarker for Bevacizumab in Colorectal Cancer Liver Metastasis: A Single-Arm, Exploratory Trial. Cancer Research and Treatment : Official Journal of Korean Cancer Association. 2016;48(4):1210–21.
104. Zabel WJ, Allam N, Foltz WD, Flueraru C, Taylor E, Vitkin IA. Bridging the macro to micro resolution gap with angiographic optical coherence tomography and dynamic contrast enhanced MRI. Sci Rep. 2022;12(1):3159.
105. Zeng Y-n, Zhang B-t, Song T, Peng J-f, Wang J-t, Yuan Q, Tan M-y: The clinical value of dynamic contrast-enhanced magnetic resonance imaging (DCE-MRI) semi-quantitative parameters in monitoring neoadjuvant chemotherapy response of osteosarcoma. Acta Radiol. 2021:02841851211030768.
106. Grøvik E, Bjørnerud A, Emblem KE. Chapter 14 - Dynamic Susceptibility Contrast MRI: Basic Physics, Pulse Sequences, and Modeling. In: Seiberlich N, Gulani V, Calamante F, Campbell-Washburn A, Doneva M, Hu HH, Sourbron S, editors. *Advances in Magnetic Resonance Technology and Applications*, vol. 1. Academic Press; 2020. p. 345–67.
107. Shiroishi MS, Castellazzi G, Boxerman JL, D'Amore F, Essig M, Nguyen TB, Provenzale JM, Enterline DS, Anzalone N, Dörfler A, et al. Principles of T2*-weighted dynamic susceptibility contrast MRI technique in brain tumor imaging. J Magn Reson Imaging. 2015;41(2):296–313.
108. Calamante F. Perfusion MRI Using Dynamic-Susceptibility Contrast MRI: Quantification Issues in Patient Studies. Top Magn Reson Imaging. 2010;21(2):75–85.
109. Essig M, Shiroishi MS, Nguyen TB, Saake M, Provenzale JM, Enterline D, Anzalone N, Dörfler A, Rovira À, Wintermark M, et al. Perfusion MRI: The Five Most Frequently Asked Technical Questions. AJR Am J Roentgenol. 2013;200(1):24–34.
110. Järnum H, Steffensen EG, Knutsson L, Fründ E-T, Simonsen CW, Lundbye-Christensen S, Shankaranarayanan A, Alsop DC, Jensen FT, Larsson E-M. Perfusion MRI of brain tumours: a comparative study of

pseudo-continuous arterial spin labelling and dynamic susceptibility contrast imaging. Neuroradiology. 2010;52(4):307–17.
111. Meier P, Zierler KL. On the theory of the indicator-dilution method for measurement of blood flow and volume. J Appl Physiol. 1954;6(12):731–44.
112. Muizelaar JP, Fatouros PP, Schröder ML. A new method for quantitative regional cerebral blood volume measurements using computed tomography. Stroke. 1997;28(10):1998–2005.
113. Schmainda KM, Zhang Z, Prah M, Snyder BS, Gilbert MR, Sorensen AG, Barboriak DP, Boxerman JL. Dynamic susceptibility contrast MRI measures of relative cerebral blood volume as a prognostic marker for overall survival in recurrent glioblastoma: results from the ACRIN 6677/RTOG 0625 multicenter trial. Neuro Oncol. 2015;17(8):1148–56.
114. Hilario A, Sepulveda JM, Hernandez-Lain A, Salvador E, Koren L, Manneh R, Ruano Y, Perez-Nuñez A, Lagares A, Ramos A. Leakage decrease detected by dynamic susceptibility-weighted contrast-enhanced perfusion MRI predicts survival in recurrent glioblastoma treated with bevacizumab. Clin Transl Oncol. 2017;19(1):51–7.
115. Schmainda KM, Prah MA, Marques H, Kim E, Barboriak DP, Boxerman JL. Value of dynamic contrast perfusion MRI to predict early response to bevacizumab in newly diagnosed glioblastoma: results from ACRIN 6686 multicenter trial. Neuro Oncol. 2021;23(2):314–23.
116. Kickingereder P, Brugnara G, Hansen MB, Nowosielski M, Pflüger I, Schell M, Isensee F, Foltyn M, Neuberger U, Kessler T, et al. Noninvasive Characterization of Tumor Angiogenesis and Oxygenation in Bevacizumab-treated Recurrent Glioblastoma by Using Dynamic Susceptibility MRI: Secondary Analysis of the European Organization for Research and Treatment of Cancer 26101 Trial. Radiology. 2020;297(1):164–75.
117. Cho HR, Kumari N, Thi VuH, Kim H, Park C-K, Choi SH. Increased Antiangiogenic Effect by Blocking CCL2-dependent Macrophages in a Rodent Glioblastoma Model: Correlation Study with Dynamic Susceptibility Contrast Perfusion MRI. Sci Rep. 2019;9(1):11085.
118. Bonekamp D, Mouridsen K, Radbruch A, Kurz FT, Eidel O, Wick A, Schlemmer H-P, Wick W, Bendszus M, Østergaard L, et al. Assessment of tumor oxygenation and its impact on treatment response in bevacizumab-treated recurrent glioblastoma. J Cereb Blood Flow Metab. 2017;37(2):485–94.
119. Le Bihan D, Breton E, Lallemand D, Grenier P, Cabanis E, Laval-Jeantet M. MR imaging of intravoxel incoherent motions: application to diffusion and perfusion in neurologic disorders. Radiology. 1986;161(2):401–7.
120. Pan JH, Zhu S, Huang J, Liang J, Zhang D, Zhao X, Ding H, Qin L, Shi C, Luo L, et al. Monitoring the Process of Endostar-Induced Tumor Vascular Normalization by Non-contrast Intravoxel Incoherent Motion Diffusion-Weighted MRI. Front Oncol. 2018;8:524.
121. Li B, Xu D, Zhou J, Wang S-C, Cai Y-X, Li H, Xu H-B: Monitoring Bevacizumab-Induced Tumor Vascular Normalization by Intravoxel Incoherent Motion Diffusion-Weighted MRI. J Magn Reson Imaging. 2021.
122. Buxton RB. The physics of functional magnetic resonance imaging (fMRI). Reports on progress in physics Physical Society (Great Britain). 2013;76(9).
123. Ogawa S, Lee TM, Kay AR, Tank DW. Brain magnetic resonance imaging with contrast dependent on blood oxygenation. Proc Natl Acad Sci USA. 1990;87(24):9868–72.
124. Liang J, Cheng Q, Huang J, Ma M, Zhang D, Lei X, Xiao Z, Zhang D, Shi C, Luo L. Monitoring tumour microenvironment changes during anti-angiogenesis therapy using functional MRI. Angiogenesis. 2019;22(3):457–70.
125. Ma M, Liang J, Zhang D, Xu X, Cheng Q, Xiao Z, Shi C, Luo L. Monitoring Treatment Efficacy of Antiangiogenic Therapy Combined With Hypoxia-Activated Prodrugs Online Using Functional MRI. Front Oncol. 2021;11:672047.
126. Sorensen AG, Batchelor TT, Zhang W-T, Chen P-J, Yeo P, Wang M, Jennings D, Wen PY, Lahdenranta J, Ancukiewicz M. A "vascular normalization index" as potential mechanistic biomarker to predict survival after a single dose of cediranib in recurrent glioblastoma patients. Cancer Res. 2009;69(13):5296–300.
127. Lusic H, Grinstaff MW. X-ray-Computed Tomography Contrast Agents. Chem Rev. 2013;113(3):1641–66.
128. Herman GT. Fundamentals of Computerized Tomography: Image Reconstruction from Projections. Springer Science & Business Media; 2009.
129. Wellington SL, Vinegar HJ. X-Ray Computerized Tomography. J Petrol Technol. 1987;39(08):885–98.
130. Nuyts J, Man BD, Fessler JA, Zbijewski W, Beekman FJ. Modelling the physics in the iterative reconstruction for transmission computed tomography. Phys Med Biol. 2013;58(12):R63–96.
131. Dendy PP, Heaton B: Physics for Diagnostic Radiology, Third Edition: CRC Press; 2011.
132. Bae KT. Intravenous Contrast Medium Administration and Scan Timing at CT: Considerations and Approaches. Radiology. 2010;256(1):32–61.
133. Hoeffner EG, Case I, Jain R, Gujar SK, Shah GV, Deveikis JP, Carlos RC, Thompson BG, Harrigan MR, Mukherji SK. Cerebral perfusion CT: technique and clinical applications. Radiology. 2004;231(3):632–44.
134. Jain R. Perfusion CT Imaging of Brain Tumors: An Overview. Am J Neuroradiol. 2011;32(9):1570–7.
135. Prezzi D, Khan A, Goh V. Perfusion CT imaging of treatment response in oncology. Eur J Radiol. 2015;84(12):2380–5.
136. Petralia G, Bonello L, Viotti S, Preda L, d'Andrea G, Bellomi M. CT perfusion in oncology: how to do it. Cancer Imaging. 2010;10(1):8–19.
137. García-Figueiras R, Goh VJ, Padhani AR, Baleato-González S, Garrido M, León L, Gómez-Caamaño A. CT Perfusion in Oncologic Imaging: A Useful Tool? Am J Roentgenol. 2013;200(1):8–19.
138. Johnson J, Wilson T. A model for capillary exchange. American Journal of Physiology-Legacy Content. 1966;210(6):1299–303.
139. Patlak CS, Blasberg RG. Graphical Evaluation of Blood-to-Brain Transfer Constants from Multiple-Time Uptake Data. J Cereb Blood Flow Metab. 1985;5(4):584–90.
140. Piperno-Neumann S, Diallo A, Etienne-Grimaldi M-C, Bidard F-C, Rodrigues M, Plancher C, Mariani P, Cassoux N, Decaudin D, Asselain B, et al. Phase II Trial of Bevacizumab in Combination With Temozolomide as First-Line Treatment in Patients With Metastatic Uveal Melanoma. Oncologist. 2016;21(3):281–282f.
141. Yao JC, Phan AT, Hess K, Fogelman D, Jacobs C, Dagohoy C, Leary C, Xie K, Ng CS. Perfusion computed tomography as functional biomarker in randomized run-in study of Bevacizumab and Everolimus in well-differentiated neuroendocrine tumors. Pancreas. 2015;44(2):190–7.
142. Kambadakone A, Yoon SS, Kim T-M, Karl DL, Duda DG, DeLaney TF, Sahani DV. CT Perfusion as an Imaging Biomarker in Monitoring Response to Neoadjuvant Bevacizumab and Radiation in Soft-Tissue Sarcomas: Comparison With Tumor Morphology, Circulating and Tumor Biomarkers, and Gene Expression. AJR Am J Roentgenol. 2015;204(1):W11–8.
143. Heist RS, Duda DG, Sahani DV, Ancukiewicz M, Fidias P, Sequist LV, Temel JS, Shaw AT, Pennell NA, Neal JW. Improved tumor vascularization after anti-VEGF therapy with carboplatin and nab-paclitaxel associates with survival in lung cancer. Proc Natl Acad Sci. 2015;112(5):1547–52.
144. Ng CS, Charnsangavej C, Wei W, Yao JC. Perfusion CT Findings in Patients With Metastatic Carcinoid Tumors Undergoing Bevacizumab and Interferon Therapy. Am J Roentgenol. 2011;196(3):569–76.
145. Tacelli N, Santangelo T, Scherpereel A, Duhamel A, Deken V, Klotz E, Cortot A, Lafitte J-J, Wallyn F, Remy J, et al. Perfusion CT allows prediction of therapy response in non-small cell lung cancer treated with conventional and anti-angiogenic chemotherapy. Eur Radiol. 2013;23(8):2127–36.
146. Aya F, Benegas M, Viñolas N, Reyes R, Vollmer I, Arcocha A, Sánchez M, Reguart N. A Pilot Study to Evaluate Early Predictive Value of Thorax Perfusion-CT in Advanced NSCLC. Cancers. 2021;13(21):5566.
147. Zou M, Zhao Z, Zhang B, Mao H, Huang Y, Wang C. Pulmonary lesions: correlative study of dynamic triple-phase enhanced CT perfusion imaging with tumor angiogenesis and vascular endothelial growth factor expression. BMC Med Imaging. 2021;21(1):158.
148. Fournier LS, Oudard S, Thiam R, Trinquart L, Banu E, Medioni J, Balvay D, Chatellier G, Frija G, Cuenod CA. Metastatic Renal Carcinoma: Evaluation of Antiangiogenic Therapy with Dynamic Contrast-enhanced CT. Radiology. 2010;256(2):511–8.
149. Jiang T, Kambadakone A, Kulkarni NM, Zhu AX, Sahani DV. Monitoring response to antiangiogenic treatment and predicting outcomes in advanced hepatocellular carcinoma using image biomarkers, CT perfusion, tumor density, and tumor size (RECIST). Invest Radiol. 2012;47(1):11–7.
150. Jia ZZ, Shi W, Shi JL, Shen DD, Gu HM, Zhou XJ. Comparison between perfusion computed tomography and dynamic contrast-enhanced

magnetic resonance imaging in assessing glioblastoma microvasculature. Eur J Radiol. 2017;87:120–4.
151. Johnson TR. Dual-Energy CT: General Principles. Am J Roentgenol. 2012;199(5_supplement):S3–8.
152. McCollough CH, Leng S, Yu L, Fletcher JG. Dual- and Multi-Energy CT: Principles, Technical Approaches, and Clinical Applications. Radiology. 2015;276(3):637–53.
153. Forghani R, De Man B, Gupta R. Dual-Energy Computed Tomography: Physical Principles, Approaches to Scanning, Usage, and Implementation: Part 1. Neuroimaging Clin N Am. 2017;27(3):371–84.
154. So A, Nicolaou S. Spectral Computed Tomography: Fundamental Principles and Recent Developments. Korean J Radiol. 2021;22(1):86–96.
155. Brodoefel H, Kramer U, Reimann A, Burgstahler C, Schroeder S, Kopp A, Heuschmid M. Dual-Source CT with Improved Temporal Resolution in Assessment of Left Ventricular Function: A Pilot Study. Am J Roentgenol. 2007;189(5):1064–70.
156. Nance JW, Bastarrika G, Kang DK, Ruzsics B, Vogt S, Schmidt B, Raupach R, Flohr TG, Schoepf UJ. High-temporal resolution dual-energy computed tomography of the heart using a novel hybrid image reconstruction algorithm: initial experience. J Comput Assist Tomogr. 2011;35(1):119–25.
157. Zhang L-J, Wu S-Y, Niu J-B, Zhang Z-L, Wang HZ, Zhao Y-E, Chai X, Zhou C-S, Lu G-M. Dual-Energy CT Angiography in the Evaluation of Intracranial Aneurysms: Image Quality, Radiation Dose, and Comparison With 3D Rotational Digital Subtraction Angiography. Am J Roentgenol. 2010;194(1):23–30.
158. Machida H, Tanaka I, Fukui R, Shen Y, Ishikawa T, Tate E, Ueno E. Dual-Energy Spectral CT: Various Clinical Vascular Applications. Radiographics. 2016;36(4):1215–32.
159. Manoharan D, Netaji A, Das CJ, Sharma S. Iodine Parameters in Triple-Bolus Dual-Energy CT Correlate With Perfusion CT Biomarkers of Angiogenesis in Renal Cell Carcinoma. Am J Roentgenol. 2020;214(4):808–16.
160. Thaiss WM, Haberland U, Kaufmann S, Spira D, Thomas C, Nikolaou K, Horger M, Sauter AW. Iodine concentration as a perfusion surrogate marker in oncology: Further elucidation of the underlying mechanisms using Volume Perfusion CT with 80 kVp. Eur Radiol. 2016;26(9):2929–36.
161. Gordic S, Puippe GD, Krauss B, Klotz E, Desbiolles L, Lesurtel M, Müllhaupt B, Pfammatter T, Alkadhi H. Correlation between Dual-Energy and Perfusion CT in Patients with Hepatocellular Carcinoma. Radiology. 2016;280(1):78–87.
162. Kang H-J, Kim SH, Bae JS, Jeon SK, Han JK. Can quantitative iodine parameters on DECT replace perfusion CT parameters in colorectal cancers? Eur Radiol. 2018;28(11):4775–82.
163. Kim YN, Lee HY, Lee KS, Seo JB, Chung MJ, Ahn M-J, Park K, Kim TS, Yi CA. Dual-Energy CT in Patients Treated with Anti-Angiogenic Agents for Non-Small Cell Lung Cancer: New Method of Monitoring Tumor Response? Korean J Radiol. 2012;13(6):702–10.
164. Han L, Huang X, Liu X, Deng Y, Ke X, Zhou Q, Zhou J. Evaluation of the anti-angiogenic effect of bevacizumab on rat C6 glioma by spectral computed tomography. Acta Radiol. 2021;62(1):120–8.
165. Lv P, Liu J, Yan X, Chai Y, Chen Y, Gao J, Pan Y, Li S, Guo H, Zhou Y. CT spectral imaging for monitoring the therapeutic efficacy of VEGF receptor kinase inhibitor AG-013736 in rabbit VX2 liver tumours. Eur Radiol. 2017;27(3):918–26.
166. Hellbach K, Sterzik A, Sommer W, Karpitschka M, Hummel N, Casuscelli J, Ingrisch M, Schlemmer M, Graser A, Staehler M. Dual energy CT allows for improved characterization of response to antiangiogenic treatment in patients with metastatic renal cell cancer. Eur Radiol. 2017;27(6):2532–7.
167. Knobloch G, Jost G, Huppertz A, Hamm B, Pietsch H. Dual-energy computed tomography for the assessment of early treatment effects of regorafenib in a preclinical tumor model: comparison with dynamic contrast-enhanced CT and conventional contrast-enhanced single-energy CT. Eur Radiol. 2014;24(8):1896–905.
168. Dai X, Schlemmer H-P, Schmidt B, Höh K, Xu K, Ganten TM, Ganten M-K. Quantitative therapy response assessment by volumetric iodine-uptake measurement: Initial experience in patients with advanced hepatocellular carcinoma treated with sorafenib. Eur J Radiol. 2013;82(2):327–34.
169. Guldberg RE, Ballock RT, Boyan BD, Duvall CL, Lin ASP, Nagaraja S, Oest M, Phillips J, Porter BD, Robertson G, et al. Analyzing bone, blood vessels, and biomaterials with microcomputed tomography. IEEE Eng Med Biol Mag. 2003;22(5):77–83.
170. Boerckel JD, Mason DE, McDermott AM, Alsberg E. Microcomputed tomography: approaches and applications in bioengineering. Stem Cell Res Ther. 2014;5(6):144.
171. Ehling J, Theek B, Gremse F, Baetke S, Möckel D, Maynard J, Ricketts S-A, Grüll H, Neeman M, Knuechel R, et al. Micro-CT Imaging of Tumor Angiogenesis: Quantitative Measures Describing Micromorphology and Vascularization. Am J Pathol. 2014;184(2):431–41.
172. Gu S, Xue J, Xi Y, Tang R, Jin W, Chen J-J, Zhang X, Shao Z-M, Wu J. Evaluating the effect of Avastin on breast cancer angiogenesis using synchrotron radiation. Quant Imaging Med Surg. 2019;9(3):418–26.
173. Hutchenreuther J, Vincent K, Norley C, Racanelli M, Gruber SB, Johnson TM, Fullen DR, Raskin L, Perbal B, Holdsworth DW, et al. Activation of cancer-associated fibroblasts is required for tumor neovascularization in a murine model of melanoma. Matrix Biol. 2018;74:52–61.
174. Omami G, Tamimi D, Branstetter BF. Basic principles and applications of 18F-FDG-PET/CT in oral and maxillofacial imaging: A pictorial essay. Imaging science in dentistry. 2014;44(4):325–32.
175. Chételat G, Arbizu J, Barthel H, Garibotto V, Law I, Morbelli S, van de Giessen E, Agosta F, Barkhof F, Brooks DJ. Amyloid-PET and 18F-FDG-PET in the diagnostic investigation of Alzheimer's disease and other dementias. Lancet Neurol. 2020;19(11):951–62.
176. Van der Geest K, Treglia G, Glaudemans A, Brouwer E, Sandovici M, Jamar F, Gheysens O, Slart RHJA. Diagnostic value of [18F] FDG-PET/CT for treatment monitoring in large vessel vasculitis: A systematic review and meta-analysis. Eur J Nucl Med Mol Imaging. 2021;48(12):3886–902.
177. Qin C, Liu F, Yen T-C, Lan X. 18F-FDG PET/CT findings of COVID-19: a series of four highly suspected cases. Eur J Nucl Med Mol Imaging. 2020;47(5):1281–6.
178. Kandathil A, Iii RCS, Subramaniam RM. Lung cancer recurrence: 18F-FDG PET/CT in clinical practice. AJR Am J Roentgenol. 2019;213(5):1136–44.
179. Dondi F, Albano D, Giubbini R, Bertagna F. 18F-FDG PET/CT for the evaluation of male breast cancer: a systematic review. Nucl Med Commun. 2022;43(2):123–8.
180. Iravani A, Hicks RJ. Imaging the cancer immune environment and its response to pharmacologic intervention, part 1: the role of 18F-FDG PET/CT. J Nucl Med. 2020;61(7):943–50.
181. Kim CG, Hwang SH, Kim KH, Yoon HI, Shim HS, Lee JH, Han Y, Ahn B-C, Hong MH, Kim HR. Predicting treatment outcomes using 18F-FDG PET biomarkers in patients with non-small-cell lung cancer receiving chemoimmunotherapy. Ther Adv Med Oncol. 2022;14:17588359211068732.
182. Liang K, Abt ER, Le TM, Cho A, Dann AM, Cui J, Li L, Rashid K, Creech AL, Wei L. STING-driven interferon signaling triggers metabolic alterations in pancreas cancer cells visualized by [18F] FLT PET imaging. Proc Natl Acad Sci USA. 2021;118(36).
183. Sharma R, Valls PO, Inglese M, Dubash S, Chen M, Gabra H, Montes A, Challapalli A, Arshad M, Tharakan G, et al. [18F] Fluciclatide PET as a biomarker of response to combination therapy of pazopanib and paclitaxel in platinum-resistant/refractory ovarian cancer. Eur J Nucl Med Mol Imaging. 2020;47(5):1239–51.
184. Kazmierczak PM, Schneider M, Habereder T, Hirner-Eppeneder H, Eschbach RS, Moser M, Reiser MF, Lauber K, Nikolaou K, Cyran CC. αvß3-Integrin–Targeted Magnetic Resonance Imaging for the Assessment of Early Antiangiogenic Therapy Effects in Orthotopic Breast Cancer Xenografts. Invest Radiol. 2016;51(11):746–55.
185. Rylova SN, Barnucz E, Fani M, Braun F, Werner M, Lassmann S, Maecke HR, Weber WA. Does imaging αvβ3 integrin expression with PET detect changes in angiogenesis during bevacizumab therapy? J Nucl Med. 2014;55(11):1878–84.
186. Shi J, Zhou Y, Chakraborty S, Kim Y-S, Jia B, Wang F, Liu S. Evaluation of 111In-labeled cyclic RGD peptides: effects of peptide and linker multiplicity on their tumor uptake, excretion kinetics and metabolic stability. Theranostics. 2011;1:322.
187. Mitsuyuki K, Watabe T, Naka S, Liu Y, Tatsumi M, Shimosegawa E, Kato H. Evaluation of Integrin αvβ3 Expression in Murine Xenograft Models:[68Ga] Ga-DOTA-C (RGDfK) PET Study with Immunohistochemical Confirmation. Diagnostics (Basel). 2021;11(7):1295.
188. Guo N, Lang L, Li W, Kiesewetter DO, Gao H, Niu G, Xie Q, Chen X. Quantitative analysis and comparison study of [18F] AlF-NOTA-PRGD2,[18F]

FPPRGD2 and [68Ga] Ga-NOTA-PRGD2 using a reference tissue model. PLoS One. 2012;7(5):e37506.
189. Li L, Ma L, Shang D, Liu Z, Yu Q, Wang S, Teng X, Zhang Q, Hu X, Zhao W, et al. Pretreatment PET/CT imaging of angiogenesis based on 18F-RGD tracer uptake may predict antiangiogenic response. Eur J Nucl Med Mol Imaging. 2019;46(4):940–7.
190. Gyuricza B, Szabó JP, Arató V, Dénes N, Szűcs Á, Berta K, Kis A, Szücs D, Forgács V, Szikra D. Synthesis of 68Ga-Labeled cNGR-Based Glycopeptides and In Vivo Evaluation by PET Imaging. Pharmaceutics. 2021;13(12):2103.
191. Pasqualini R, Koivunen E, Kain R, Lahdenranta J, Sakamoto M, Stryhn A, Ashmun RA, Shapiro LH, Arap W. Ruoslahti EJCr: Aminopeptidase N is a receptor for tumor-homing peptides and a target for inhibiting angiogenesis. 2000;60(3):722–7.
192. Bekaert L, Valable S, Lechapt-Zalcman E, Ponte K, Collet S, Constans J-M, Levallet G, Bordji K, Petit E, Branger P, et al. [18F]-FMISO PET study of hypoxia in gliomas before surgery: correlation with molecular markers of hypoxia and angiogenesis. Eur J Nucl Med Mol Imaging. 2017;44:1383–92.
193. Hernández-Agudo E, Mondejar T, Soto-Montenegro ML, Megías D, Mouron S, Sanchez J, Hidalgo M, Lopez-Casas PP, Mulero F, Desco M. Monitoring vascular normalization induced by antiangiogenic treatment with 18F-fluoromisonidazole-PET. Mol Oncol. 2016;10(5):704–18.
194. Quintela-Fandino M, Lluch A, Manso L, Calvo I, Cortes J, García-Saenz JA, Gil-Gil M, Martinez-Jánez N, Gonzalez-Martin A, Adrover E. 18F-fluoromisonidazole PET and activity of neoadjuvant nintedanib in early HER2-negative breast cancer: a window-of-opportunity randomized trial. Clin Cancer Res. 2017;23(6):1432–41.
195. Fragomeni RAS, Amir T, Sheikhbahaei S, Harvey SC, Javadi MS, Solnes LB, Kiess AP, Allaf ME, Pomper MG, Gorin MA. Imaging of nonprostate cancers using PSMA-targeted radiotracers: rationale, current state of the field, and a call to arms. J Nucl Med. 2018;59(6):871–7.
196. Medina-Ornelas S, García-Perez F, Estrada-Lobato E, Ochoa-Carrillo F. 68Ga-PSMA PET/CT in the evaluation of locally advanced and metastatic breast cancer, a single center experience. Am J Nucl Med Mol Imaging. 2020;10(3):135–42.
197. Sathekge M, Lengana T, Modiselle M, Vorster M, Zeevaart J, Maes A, Ebenhan T, Van de Wiele C. 68 Ga-PSMA-HBED-CC PET imaging in breast carcinoma patients. Eur J Nucl Med Mol Imaging. 2017;44:689–94.
198. Cuda TJ, Riddell AD, Liu C, Whitehall VL, Borowsky J, Wyld DK, Burge ME, Ahern E, Griffin A, Lyons NJR. PET imaging quantifying 68Ga-PSMA-11 uptake in metastatic colorectal cancer. J Nucl Med. 2020;61(11):1576–9.
199. Hangaard L, Jochumsen MR, Vendelbo MH, Bouchelouche K. Metastases from colorectal cancer avid on 68Ga-PSMA PET/CT. Clin Cancer Res. 2017;42(7):532–3.
200. Rhee H, Blazak J, Tham CM, Ng KL, Shepherd B, Lawson M, Preston J, Vela I, Thomas P, Wood S. Pilot study: use of gallium-68 PSMA PET for detection of metastatic lesions in patients with renal tumour. EJNMMI Res. 2016;6:1–6.
201. Aggarwal P, Singh H, Das CK, Mavuduru RS, Kakkar N, Lal A, Gorsi U, Kumar R, Mittal BR. Potential role of 68Ga-PSMA PET/CT in metastatic renal cell cancer: A prospective study. Eur J Radiol. 2024;170.
202. Kunikowska J, Bartosz K, Leszek K. Glioblastoma multiforme: another potential application for 68 Ga-PSMA PET/CT as a guide for targeted therapy. Eur J Nucl Med Mol Imaging. 2018;45:886–7.
203. Sasikumar A, Kashyap R, Joy A, Patro KC, Bhattacharya P, Pilaka VKR, Oommen KE, Pillai MRA. Utility of 68Ga-PSMA-11 PET/CT in imaging of glioma—a pilot study. Clin Nucl Med. 2018;43(9):e304–9.
204. Lütje S, Gomez B, Cohnen J, Umutlu L, Gotthardt M, Poeppel TD, Bockisch A, Rosenbaum-Krumme S. Imaging of prostate-specific membrane antigen expression in metastatic differentiated thyroid cancer using 68Ga-HBED-CC-PSMA PET/CT. Clin Nucl Med. 2017;42(1):20–5.
205. de Vries LH, Lodewijk L, Braat AJ, Krijger GC, Valk GD, Lam MG, Borel Rinkes IH, Vriens MR, de Keizer B. 68 Ga-PSMA PET/CT in radioactive iodine-refractory differentiated thyroid cancer and first treatment results with 177 Lu-PSMA-617. EJNMMI Res. 2020;10:1–8.
206. Krishnaraju VS, Kumar R, Mittal BR, Sharma V, Singh H, Nada R, Bal A, Rohilla M, Singh H, Rana SS. Differentiating benign and malignant pancreatic masses: Ga-68 PSMA PET/CT as a new diagnostic avenue. Eur Radiol. 2021;31:2199–208.
207. Thompson SM, Suman G, Torbenson MS, Chen ZME, Jondal DE, Patra A, Ehman EC, Andrews JC, Fleming CJ, Welch BT. PSMA as a Theranostic Target in Hepatocellular Carcinoma: Immunohistochemistry and 68Ga-PSMA-11 PET Using Cyclotron-Produced 68Ga. Hepatol Commun. 2022;6(5):1172–85.
208. Backhaus P, Noto B, Avramovic N, Grubert LS, Huss S, Bögemann M, Stegger L, Weckesser M, Schaefers M, Rahbar K, et al. Targeting PSMA by radioligands in non-prostate disease—current status and future perspectives. Eur J Nucl Med Mol Imaging. 2018;45:860–77.
209. de Galiza BF, Queiroz MA, Nunes RF, Costa LB, Zaniboni EC, Marin JFG, Cerri GG. Buchpiguel CAJCI: Nonprostatic diseases on PSMA PET imaging: a spectrum of benign and malignant findings. 2020;20:1–23.
210. Sollini M, di Tommaso L, Kirienko M, Piombo C, Erreni M, Lania AG, Erba PA, Antunovic L. Chiti AJEr: PSMA expression level predicts differentiated thyroid cancer aggressiveness and patient outcome. 2019;9:1–13.
211. Marafi F, Sasikumar A, Alfeeli M, Fathallah W. 18F-PSMA 1007 uptake in brain metastases from breast cancer. Clin Nucl Med. 2020;45(2):e77–9.
212. Passah A, Arora S, Damle NA, Tripathi M, Bal C, Subudhi TK, Arora G. 68Ga–Prostate-Specific Membrane Antigen PET/CT in Triple-Negative Breast Cancer. Clin Nucl Med. 2018;43(6):460–1.
213. Voter AF, Werner RA, Pienta KJ, Gorin MA, Pomper MG, Solnes LB, Rowe SP. Piflufolastat F-18 (18F-DCFPyL) for PSMA PET imaging in prostate cancer. Expert Rev Anticancer Ther. 2022;22(7):681–94.
214. Rasul S, Haug ARJC. Clinical applications of PSMA PET examination in patients with prostate cancer. Cancers (Basel). 2022;14(15):3768.
215. Akdemir EN, Tuncel M, Akyol F, Bilen CY, Baydar DE, Karabulut E, Ozen H, Caglar M. 68 Ga-labelled PSMA ligand HBED-CC PET/CT imaging in patients with recurrent prostate cancer. World J Urol. 2019;37:813–21.
216. Santhanam P, Russell J, Rooper LM, Ladenson PW, Pomper MG, Rowe SP. The prostate-specific membrane antigen (PSMA)-targeted radiotracer 18 F-DCFPyL detects tumor neovasculature in metastatic, advanced, radioiodine-refractory, differentiated thyroid cancer. Med Oncol. 2020;37:1–7.
217. Sanchez-Crespo A. Isotopes: Comparison of Gallium-68 and Fluorine-18 imaging characteristics in positron emission tomography. Appl Radiat Isot. 2013;76:55–62.
218. Tsechelidis I, Vrachimis A. PSMA PET in imaging prostate cancer. Front Oncol. 2022;12:831429.
219. Braune A, Hofheinz F, Bluth T, Kiss T, Wittenstein J, Scharffenberg M, Kotzerke J, de Abreu MG. Comparison of static and dynamic 18F-FDG PET/CT for quantification of pulmonary inflammation in acute lung injury. J Nucl Med. 2019;60(11):1629–34.
220. Tomasi G, Turkheimer F, Aboagye E. Importance of quantification for the analysis of PET data in oncology: review of current methods and trends for the future. Mol Imag Biol. 2012;14:131–46.
221. Dimitrakopoulou-Strauss A, Pan L, Sachpekidis C. Kinetic modeling and parametric imaging with dynamic PET for oncological applications: general considerations, current clinical applications, and future perspectives. Eur J Nucl Med Mol Imaging. 2021;48:21–39.
222. Niu G, Chen X. PET imaging of angiogenesis. PET Clin. 2009;4(1):17–38.
223. Greig EC, Duker JS, Waheed NK. A practical guide to optical coherence tomography angiography interpretation. Int J Retin Vitreous. 2020;6(1):55.
224. Spaide RF, Fujimoto JG, Waheed NK, Sadda SR, Staurenghi G. Optical coherence tomography angiography. Prog Retin Eye Res. 2018;64:1–55.
225. Theotoka D, Liu Z, Wall S, Galor A, Al Bayyat GJ, Feuer W, Jianhua W, Karp CL. Optical coherence tomography angiography in the evaluation of vascular patterns of ocular surface squamous neoplasia during topical medical treatment. Ocul Surf. 2022;25:8–18.
226. Spaide RF. Optical Coherence Tomography Angiography Signs of Vascular Abnormalization With Antiangiogenic Therapy for Choroidal Neovascularization. Am J Ophthalmol. 2015;160(1):6–16.
227. Deegan AJ, Talebi-Liasi F, Song S, Li Y, Xu J, Men S, Shinohara MM, Flowers ME, Lee SJ, Wang RK. Optical coherence tomography angiography of normal skin and inflammatory dermatologic conditions. Lasers Surg Med. 2018;50(3):183–93.
228. Li Y, Zhu Y, Zhang F, Tang J, Mehrabi J, Kelly K, Chen Z: 1.7-micron optical coherence tomography angiography for characterization of skin cancer. In: Photonics in Dermatology and Plastic Surgery 2021: 2021-3-5 2021: SPIE; 2021: 5.

229. Hielscher AH, Bluestone AY, Abdoulaev GS, Klose AD, Lasker J, Stewart M, Netz U, Beuthan J. Near-Infrared Diffuse Optical Tomography. Dis Markers. 2002;18(5–6):313–37.
230. Zhu Q, Kurtzman SH, Hegde P, Tannenbaum S, Kane M, Huang M, Chen NG, Jagjivan B, Zarfos K. Utilizing Optical Tomography with Ultrasound Localization to Image Heterogeneous Hemoglobin Distribution in Large Breast Cancers. Neoplasia. 2005;7(3):263–70.
231. Zhu Q, Tannenbaum S, Kurtzman SH. Optical Tomography with Ultrasound Localization for Breast Cancer Diagnosis and Treatment Monitoring. Surg Oncol Clin N Am. 2007;16(2):307–21.
232. Pogue BW, Poplack SP, McBride TO, Wells WA, Osterman KS, Osterberg UL, Paulsen KD. Quantitative Hemoglobin Tomography with Diffuse Near-Infrared Spectroscopy: Pilot Results in the Breast. Radiology. 2001;218(1):261–6.
233. Ntziachristos V, Yodh AG, Schnall MD, Chance B. MRI-Guided Diffuse Optical Spectroscopy of Malignant and Benign Breast Lesions. Neoplasia. 2002;4(4):347–54.
234. Flexman ML, Vlachos F, Kim HK, Sirsi SR, Huang J, Hernandez SL, Johung TB, Gander JW, Reichstein AR, Lampl BS. Monitoring early tumor response to drug therapy with diffuse optical tomography. J Biomed Opt. 2012;17(1):016014–016014.
235. Fugazza A, Gaiani F, Carra MC, Brunetti F, Lévy M, Sobhani I, Azoulay D, Catena F. de'Angelis GL, de'Angelis N: Confocal Laser Endomicroscopy in Gastrointestinal and Pancreatobiliary Diseases: A Systematic Review and Meta-Analysis. Biomed Res Int. 2016;2016:1–31.
236. De Palma GD, Maione F, Esposito D, Luglio G, Giglio MC, Siciliano S, Gennarelli N, Cassese G, Campione S, D'Armiento FP, et al. *In vivo* assessment of tumour angiogenesis in colorectal cancer: the role of confocal laser endomicroscopy. Colorectal Dis. 2016;18(2):O66–73.
237. Liu H, Li Y-Q, Yu T, Zhao Y-A, Zhang J-P, Zhang J-N, Guo Y-T, Xie X-J, Zhang T-G, Desmond PV: Confocal endomicroscopy for in vivo detection of microvascular architecture in normal and malignant lesions of upper gastrointestinal tract. J Gastroenterol Hepatol. 2007;071119181347002
238. Meining A, Frimberger E, Becker V, Delius SV, Weyhern CHV, Schmid RM, Prinz C. Detection of Cholangiocarcinoma In Vivo Using Miniprobe-Based Confocal Fluorescence Microscopy. Clin Gastroenterol Hepatol. 2008;6(9):1057–60.
239. Chen SP, Liao JC. Confocal Laser Endomicroscopy of Bladder and Upper Tract Urothelial Carcinoma: A New Era of Optical Diagnosis? Curr Urol Rep. 2014;15(9):437.
240. Cârțână T, Săftoiu A, Gruionu LG, Gheonea DI, Pirici D, Georgescu CV, Ciocâlteu A, Gruionu G. Confocal laser endomicroscopy for the morphometric evaluation of microvessels in human colorectal cancer using targeted anti-CD31 antibodies. PLoS One. 2012;7(12).
241. Paull PE, Hyatt BJ, Wassef W, Fischer AH. Confocal Laser Endomicroscopy: A Primer for Pathologists. Arch Pathol Lab Med. 2011;135(10):1343–8.
242. Xi G, Cao N, Guo W, Kang D, Chen Z, He J, Ren W, Shen T, Wang C, Chen J. Label-free imaging of blood vessels in human normal breast and breast tumor tissue using multiphoton microscopy. Scanning. 2019;(1):5192875.
243. Brown EB, Campbell RB, Tsuzuki Y, Xu L, Carmeliet P, Fukumura D, Jain RK. In vivo measurement of gene expression, angiogenesis and physiological function in tumors using multiphoton laser scanning microscopy. Nat Med. 2001;7(7):864–8.
244. Ricard C, Debarbieux FC. Six-color intravital two-photon imaging of brain tumors and their dynamic microenvironment. Front Cell Neurosci. 2014;8:57.
245. Wang S, Liu J, Goh CC, Ng LG, Liu B. NIR-II-Excited Intravital Two-Photon Microscopy Distinguishes Deep Cerebral and Tumor Vasculatures with an Ultrabright NIR-I AIE Luminogen. Adv Mater. 2019;31(44):1904447.
246. Maurin M, Stéphan O, Vial J-C, Marder SR, van der Sanden B. Deep in vivo two-photon imaging of blood vessels with a new dye encapsulated in pluronic nanomicelles. J Biomed Opt. 2011;16(3): 036001.
247. Chen L, Chen M, Zhou Y, Ye C, Liu R. NIR Photosensitizer for Two-Photon Fluorescent Imaging and Photodynamic Therapy of Tumor. Front Chem. 2021;9: 629062.
248. Li Y, Tang R, Liu X, Gong J, Zhao Z, Sheng Z, Zhang J, Li X, Niu G, Kwok RTK, et al. Bright Aggregation-Induced Emission Nanoparticles for Two-Photon Imaging and Localized Compound Therapy of Cancers. ACS Nano. 2020;14(12):16840–53.
249. Yoon H-J, Lee E-S, Kang M, Jeong Y, Park J-H. In vivo multi-photon luminescence imaging of cerebral vasculature and blood–brain barrier integrity using gold nanoparticles. J Mater Chem B. 2015;3(15):2935–8.
250. Fan JL, Rivera JA, Sun W, Peterson J, Haeberle H, Rubin S, Ji N. High-speed volumetric two-photon fluorescence imaging of neurovascular dynamics. Nat Commun. 2020;11(1):6020.
251. Konig K. Multiphoton microscopy in life sciences. J Microsc. 2000;200(2):83–104.
252. Klauser A, Frauscher F, Schirmer M, Halpern E, Pallwein L, Herold M, Helweg G, ZurNedden D. The value of contrast-enhanced color Doppler ultrasound in the detection of vascularization of finger joints in patients with rheumatoid arthritis. Arthritis Rheum. 2002;46(3):647–53.
253. Girlich C, Schacherer D, Jung E, Schreyer A, Büttner R. Comparison between a clinical activity index (Harvey–Bradshaw-Index), laboratory inflammation markers and quantitative assessment of bowel wall vascularization by contrast-enhanced ultrasound in Crohn's disease. Eur J Radiol. 2012;81(6):1105–9.
254. Lindner JR. Contrast ultrasound molecular imaging of inflammation in cardiovascular disease. Cardiovasc Res. 2009;84(2):182–9.
255. Stein JH, Korcarz CE, Hurst RT, Lonn E, Kendall CB, Mohler ER, Najjar SS, Rembold CM, Post WS. Use of carotid ultrasound to identify subclinical vascular disease and evaluate cardiovascular disease risk: a consensus statement from the American Society of Echocardiography Carotid Intima-Media Thickness Task Force endorsed by the Society for Vascular Medicine. J Am Soc Echocardiogr. 2008;21(2):93–111.
256. Haymart MR, Banerjee M, Reyes-Gastelum D, Caoili E, Norton EC. Thyroid ultrasound and the increase in diagnosis of low-risk thyroid cancer. J Clin Endocrinol Metab. 2019;104(3):785–92.
257. Sood R, Rositch AF, Shakoor D, Ambinder E, Pool K-L, Pollack E, Mollura DJ, Mullen LA, Harvey SC. Ultrasound for breast cancer detection globally: a systematic review and meta-analysis. J Glob Oncol. 2019;5:1–17.
258. Kamal R, Hamed S, Mansour S, Mounir Y, Abdel Sallam S. Ovarian cancer screening—ultrasound; impact on ovarian cancer mortality. Br J Radiol. 2018;91(1090):20170571.
259. Unger EC, Porter T, Culp W, Labell R, Matsunaga T, Zutshi R. Therapeutic applications of lipid-coated microbubbles. Adv Drug Deliv Rev. 2004;56(9):1291–314.
260. Lindner JR. Microbubbles in medical imaging: current applications and future directions. Nat Rev Drug Discov. 2004;3(6):527–33.
261. Wei K, Jayaweera AR, Firoozan S, Linka A, Skyba DM, Kaul SJC. Quantification of myocardial blood flow with ultrasound-induced destruction of microbubbles administered as a constant venous infusion. Circulation. 1998;97(5):473–83.
262. Faccia M, Garcovich M, Ainora ME, Riccardi L, Pompili M, Gasbarrini A, Zocco MA. Contrast-Enhanced Ultrasound for Monitoring Treatment Response in Different Stages of Hepatocellular Carcinoma. Cancers (Basel). 2022;14(3):481.
263. Korpanty G, Carbon JG, Grayburn PA, Fleming JB, Brekken RA. Monitoring response to anticancer therapy by targeting microbubbles to tumor vasculature. Clin Cancer Res. 2007;13(1):323–30.
264. Brahimi-Horn MC, Chiche J, Pouysségur J. Hypoxia and cancer. J Mol Med. 2007;85(12):1301–7.
265. Dietrich C, Averkiou M, Correas J-M, Lassau N, Leen E, Piscaglia F. An EFSUMB introduction into Dynamic Contrast-Enhanced Ultrasound (DCE-US) for quantification of tumour perfusion. Ultraschall in der Medizin-European Journal of Ultrasound. 2012;33(04):344–51.
266. Lassau N, Chami L, Chebil M, Benatsou B, Bidault S, Girard E, Abboud G, Roche A. Dynamic contrast-enhanced ultrasonography (DCE-US) and anti-angiogenic treatments. Discov Med. 2011;11(56):18–24.
267. Minami Y, Kudo M. Review of dynamic contrast-enhanced ultrasound guidance in ablation therapy for hepatocellular carcinoma. World J Gastroenterol. 2011;17(45):4952.
268. Cosgrove D, Lassau N. Imaging of perfusion using ultrasound. Eur J Nucl Med Mol Imaging. 2010;37(1):65–85.
269. Lassau N, Chebil M, Chami L, Bidault S, Girard E, Roche A. Dynamic contrast-enhanced ultrasonography (DCE-US): a new tool for the early evaluation of antiangiogenic treatment. Target Oncol. 2010;5(1):53–8.
270. Lassau N: Advanced Ultrasound Imaging for Patients in Oncology: DCE-US. In: Molecular Imaging in Oncology. edn.: Springer; 2020: 765-771.

271. Lassau N, Chapotot L, Benatsou B, Vilgrain V, Kind M, Lacroix J, Cuinet M, Taieb S, Aziza R, Sarran A. Standardization of dynamic contrast-enhanced ultrasound for the evaluation of antiangiogenic therapies: the French multicenter Support for Innovative and Expensive Techniques Study. Invest Radiol. 2012;47(12):711–6.
272. Lassau N, Bonastre J, Kind M, Vilgrain V, Lacroix J, Cuinet M, Taieb S, Aziza R, Sarran A, Labbe-Devilliers C. Validation of dynamic contrast-enhanced ultrasound in predicting outcomes of antiangiogenic therapy for solid tumors: the French multicenter support for innovative and expensive techniques study. Invest Radiol. 2014;49(12):794.
273. Lassau N, Chami L, Chebil M, Benatsou B, Bidault S, Girard E, Abboud G, Roche A. Dynamic contrast-enhanced ultrasonography (DCE-US) and anti-angiogenic treatments. Discov Med. 2011;11(56):18–24.
274. Pitre-Champagnat S, Leguerney I, Bosq J, Peronneau P, Kiessling F, Calmels L, Coulot J, Lassau N. Dynamic contrast-enhanced ultrasound parametric maps to evaluate intratumoral vascularization. Invest Radiol. 2015;50(4):212–7.
275. Wu S-K, Chu P-C, Chai W-Y, Kang S-T, Tsai C-H, Fan C-H, Yeh C-K, Liu H-L. Characterization of different microbubbles in assisting focused ultrasound-induced blood-brain barrier opening. Sci Rep. 2017;7(1):1–11.
276. Newsome IG, Dayton PA: Acoustic Angiography: Superharmonic Contrast-Enhanced Ultrasound Imaging for Noninvasive Visualization of Microvasculature. In: Biomedical Engineering Technologies. edn.: Springer; 2022: 641-655.
277. Bouakaz A, Frigstad S, Ten Cate FJ, de Jong N. Super harmonic imaging: a new imaging technique for improved contrast detection. Ultrasound Med Biol. 2002;28(1):59–68.
278. Shelton SE, Lee YZ, Lee M, Cherin E, Foster FS, Aylward SR, Dayton PA. Quantification of microvascular tortuosity during tumor evolution using acoustic angiography. Ultrasound Med Biol. 2015;41(7):1896–904.
279. Shelton SE, Stone J, Gao F, Zeng D, Dayton PA: Microvascular ultrasonic imaging of angiogenesis identifies tumors in a murine spontaneous breast cancer model. 2020;2020.
280. Gessner RC, Aylward SR, Dayton PA. Mapping microvasculature with acoustic angiography yields quantifiable differences between healthy and tumor-bearing tissue volumes in a rodent model. Radiology. 2012;264(3):733–40.
281. Kasoji SK, Rivera JN, Gessner RC, Chang SX, Dayton PA. Early assessment of tumor response to radiation therapy using high-resolution quantitative microvascular ultrasound imaging. Theranostics. 2018;8(1):156.
282. Taruttis A, van Dam GM, Ntziachristos V. Mesoscopic and macroscopic optoacoustic imaging of cancer. Cancer Res. 2015;75(8):1548–59.
283. Panfilova A, Shelton SE, Caresio C, van Sloun RJ, Molinari F, Wijkstra H, Dayton PA, Mischi M. On the relationship between dynamic contrast-enhanced ultrasound parameters and the underlying vascular architecture extracted from acoustic angiography. Ultrasound Med Biol. 2019;45(2):539–48.
284. Rojas JD, Papadopoulou V, Czernuszewicz TJ, Rajamahendiran RM, Chytil A, Chiang Y-C, Chong DC, Bautch VL, Rathmell WK, Aylward S. Ultrasound measurement of vascular density to evaluate response to anti-angiogenic therapy in renal cell carcinoma. IEEE Trans Biomed Eng. 2018;66(3):873–80.
285. Mahmud MM, Adelegan OJ, Sanders JL, Zhang X, Yamaner FY, Dayton PA, Oralkan Ö: Improved CMUT structure and method of operation for dual-frequency acoustic angiography. In: 2017 IEEE International Ultrasonics Symposium (IUS): 2017: IEEE; 2017: 1-4.
286. Newsome IG, Kierski TM, Pang G, Yin J, Yang J, Carnevale C, Foster FS, Cherin E, Demore CE, Dayton PA: Enhanced depth of field acoustic angiography with a prototype 288-element dual-frequency array. In: 2019 IEEE International Ultrasonics Symposium (IUS): 2019: IEEE; 2019: 1941-1943.
287. Cherin E, Yin J, Forbrich A, White C, Dayton PA, Foster FS, Démoré CEM. In vitro superharmonic contrast imaging using a hybrid dual-frequency probe. Ultrasound Med Biol. 2019;45(9):2525–39.
288. Jain RK, Fukumura D: Angiogenesis in Development, Disease, and Regeneration. In: Strategies in Regenerative Medicine: Integrating Biology with Materials Design. edn.: Springer; 2008: 1-41.
289. Chang Y-C, Huang Y-H, Huang C-S, Chang R-F. Vascular morphology and tortuosity analysis of breast tumor inside and outside contour by 3-D power Doppler ultrasound. Ultrasound Med Biol. 2012;38(11):1859–69.
290. Demené C, Payen T, Dizeux A, Barrois G, Gennisson J-L, Bridal L, Tanter M. 3-D longitudinal imaging of tumor angiogenesis in mice in vivo using ultrafast Doppler tomography. Ultrasound Med Biol. 2019;45(5):1284–96.
291. Wang H, Yan B, Yue L, He M, Liu Y, Li H. The diagnostic value of 3d power doppler ultrasound combined with vocal in the vascular distribution of breast masses. Acad Radiol. 2020;27(2):198–203.
292. Abdollahi A, Lipson KE, Sckell A, Zieher H, Klenke F, Poerschke D, Roth A, Han X, Krix M, Bischof M. Combined therapy with direct and indirect angiogenesis inhibition results in enhanced antiangiogenic and antitumor effects. Cancer Res. 2003;63(24):8890–8.
293. Goertz DE, Yu JL, Kerbel RS, Burns PN, Foster FS. High-frequency Doppler ultrasound monitors the effects of antivascular therapy on tumor blood flow. Cancer Res. 2002;62(22):6371–5.
294. Palmowski M, Huppert J, Hauff P, Reinhardt M, Schreiner K, Socher MA, Hallscheidt P, Kauffmann GW, Semmler W, Hallscheidt P, Kauffmann GW, Semmler W, Kiessling F. Vessel fractions in tumor xenografts depicted by flow-or contrast-sensitive three-dimensional high-frequency Doppler ultrasound respond differently to antiangiogenic treatment. Cancer Res. 2008;68(17):7042–9.
295. Rix A, Lederle W, Siepmann M, Fokong S, Behrendt FF, Bzyl J, Grouls C, Kiessling F, Palmowski M. Evaluation of high frequency ultrasound methods and contrast agents for characterising tumor response to anti-angiogenic treatment. Eur J Radiol. 2012;81(10):2710–6.
296. Jugold M, Palmowski M, Huppert J, Woenne EC, Mueller MM, Semmler W, Kiessling F. Volumetric high-frequency Doppler ultrasound enables the assessment of early antiangiogenic therapy effects on tumor xenografts in nude mice. Eur Radiol. 2008;18:753–8.
297. Huang C, Lowerison MR, Lucien F, Gong P, Wang D, Song P, Chen S. Noninvasive contrast-free 3D evaluation of tumor angiogenesis with ultrasensitive ultrasound microvessel imaging. Sci Rep. 2019;9(1):1–11.
298. Demené C, Deffieux T, Pernot M, Osmanski B-F, Biran V, Gennisson J-L, Sieu L-A, Bergel A, Franqui S, Correas J-M. Spatiotemporal clutter filtering of ultrafast ultrasound data highly increases Doppler and fUltrasound sensitivity. IEEE Trans Med Imaging. 2015;34(11):2271–85.
299. Christensen-Jeffries K, Browning RJ, Tang M-X, Dunsby C. In vivo acoustic super-resolution and super-resolved velocity mapping using microbubbles. IEEE Trans Med Imaging. 2014;34(2):433–40.
300. Ghosh D, Xiong F, Sirsi SR, Mattrey R, Brekken R, Kim J-W, Hoyt K: Monitoring early tumor response to vascular targeted therapy using super-resolution ultrasound imaging. In: 2017 IEEE international ultrasonics symposium (Ius): 2017: IEEE; 2017: 1-4.
301. Yu J, Lavery L. Kim KJSr: Super-resolution ultrasound imaging method for microvasculature in vivo with a high temporal accuracy. 2018;8(1):1–11.
302. Brown KG. Ghosh D. Hoyt KJItou, ferroelectrics, control f: Deep learning of spatiotemporal filtering for fast super-resolution ultrasound imaging. 2020;67(9):1820–9.
303. Brown KG, Waggener SC. Redfern AD. Hoyt KJBp, express e: Faster super-resolution ultrasound imaging with a deep learning model for tissue decluttering and contrast agent localization. 2021;7(6): 065035.
304. Attia ABE, Balasundaram G, Moothanchery M, Dinish U, Bi R, Ntziachristos V, Olivo MJP. A review of clinical photoacoustic imaging: Current and future trends. 2019;16: 100144.
305. Yang Z, Chen J, Yao J, Lin R, Meng J, Liu C, Yang J, Li X, Wang L. Song LJOe: Multi-parametric quantitative microvascular imaging with optical-resolution photoacoustic microscopy in vivo. 2014;22(2):1500–11.
306. Ahn J, Kim JY, Choi W, Kim CJP. High-resolution functional photoacoustic monitoring of vascular dynamics in human fingers. 2021;23: 100282.
307. Yao J, Wang L, Yang J-M, Maslov KI, Wong TT, Li L, Huang C-H, Zou J. Wang LVJNm: High-speed label-free functional photoacoustic microscopy of mouse brain in action. 2015;12(5):407–10.
308. Hu S. Wang LVJBj: Optical-resolution photoacoustic microscopy: auscultation of biological systems at the cellular level. 2013;105(4):841–7.
309. Jeon S, Kim J, Lee D, Baik JW, Kim CJP. Review on practical photoacoustic microscopy. 2019;15: 100141.
310. Hai P, Yao J, Maslov KI, Zhou Y. Wang LVJOl: Near-infrared optical-resolution photoacoustic microscopy. 2014;39(17):5192–5.
311. Zhang X, Liu Y, Tao C, Yin J, Hu Z, Yuan S, Liu Q, Liu X: High-Sensitivity Optical-Resolution Photoacoustic Microscopy with an Optical-Acoustic

Combiner Based on an Off-Axis Parabolic Acoustic Mirror. In: Photonics: 2021: Multidisciplinary Digital Publishing Institute; 2021: 127.
312. Bi R, Dinish U, Goh CC, Imai T, Moothanchery M, Li X, Kim JY, Jeon S, Pu Y. Kim CJJob: In vivo label-free functional photoacoustic monitoring of ischemic reperfusion. 2019;12(7): e201800454.
313. Zhao J, Zhao Q, Lin R. Meng JJJoIOHS: A microvascular image analysis method for optical-resolution photoacoustic microscopy. 2020;13(04):2050019.
314. Chen M, Duan X, Lan B, Vu T, Zhu X, Rong Q, Yang W, Hoffmann U, Zou J, Yao JJP. High-speed functional photoacoustic microscopy using a water-immersible two-axis torsion-bending scanner. 2021;24: 100309.
315. Park K, Kim JY, Lee C, Jeon S, Lim G. Kim CJSr: Handheld photoacoustic microscopy probe. 2017;7(1):1–15.
316. Hu S, Maslov KI, Tsytsarev V. Wang LVJJobo: Functional transcranial brain imaging by optical-resolution photoacoustic microscopy. 2009;14(4): 040503.
317. Mirg S, Chen H, Turner KL, Gheres KW, Liu J, Gluckman BJ, Drew PJ. Kothapalli S-RJOL: Awake mouse brain photoacoustic and optical imaging through a transparent ultrasound cranial window. 2022;47(5):1121–4.
318. Zhou H-C, Chen N, Zhao H, Yin T, Zhang J, Zheng W, Song L, Liu C, Zheng RJP. Optical-resolution photoacoustic microscopy for monitoring vascular normalization during anti-angiogenic therapy. 2019;15: 100143.
319. Rao B, Leng X, Zeng Y, Lin Y, Chen R, Zhou Q, Hagemann AR, Kuroki LM, McCourt CK. Mutch DGJSr: Optical resolution photoacoustic microscopy of ovary and fallopian tube. 2019;9(1):1–9.
320. Zhang HF, Maslov K. Wang LVJNp: In vivo imaging of subcutaneous structures using functional photoacoustic microscopy. 2007;2(4):797–804.
321. Seong M. Chen S-LJSCLS: Recent advances toward clinical applications of photoacoustic microscopy: a review. 2020;63(12):1798–812.
322. Hu S. Wang LVJJobo: Photoacoustic imaging and characterization of the microvasculature. 2010;15(1): 011101.
323. Wang L, Maslov K, Yao J, Rao B. Wang LVJOl: Fast voice-coil scanning optical-resolution photoacoustic microscopy. 2011;36(2):139–41.
324. Wang L, Maslov K. Wang LVJPotNAoS: Single-cell label-free photoacoustic flowoxigraphy in vivo. 2013;110(15):5759–64.
325. Omar M, Aguirre J. Ntziachristos VJNbe: Optoacoustic mesoscopy for biomedicine. 2019;3(5):354–70.
326. Omar M, Soliman D, Gateau J. Ntziachristos VJOl: Ultrawideband reflection-mode optoacoustic mesoscopy. 2014;39(13):3911–4.
327. Haedicke K, Agemy L, Omar M, Berezhnoi A, Roberts S, Longo-Machado C, Skubal M, Nagar K, Hsu H-T, Kim K. High-resolution optoacoustic imaging of tissue responses to vascular-targeted therapies. Nature biomedical engineering. 2020;4(3):286–97.
328. Orlova A, Sirotkina M, Smolina E, Elagin V, Kovalchuk A, Turchin I, Subochev PJP. Raster-scan optoacoustic angiography of blood vessel development in colon cancer models. 2019;13:25–32.
329. Haedicke K, Agemy L, Omar M, Berezhnoi A, Roberts S, Longo-Machado C, Skubal M, Nagar K, Hsu H-T. Kim KJNbe: High-resolution optoacoustic imaging of tissue responses to vascular-targeted therapies. 2020;4(3):286–97.
330. Lao Y, Xing D. Yang S. Xiang LJPiM, Biology: Noninvasive photoacoustic imaging of the developing vasculature during early tumor growth. 2008;53(15):4203.
331. Bohndiek SE, Sasportas LS, Machtaler S, Jokerst JV, Hori S, Gambhir SS. Photoacoustic tomography detects early vessel regression and normalization during ovarian tumor response to the antiangiogenic therapy trebananib. J Nucl Med. 2015;56(12):1942–7.
332. Taruttis A, Timmermans AC, Wouters PC, Kacprowicz M, van Dam GM, Ntziachristos VJR. Optoacoustic imaging of human vasculature: feasibility by using a handheld probe. 2016;281(1):256–63.
333. Rich LJ, Seshadri MJR. Photoacoustic imaging of vascular hemodynamics: validation with blood oxygenation level–dependent MR imaging. Radiology. 2015;275(1):110–8.
334. Walsh JC, Kolb HC. The clinical importance of assessing tumor hypoxia: relationship of tumor hypoxia to prognosis and therapeutic opportunities. Antioxid Redox Signal. 2014;21(10):1516–54.
335. Matsumoto Y, Asao Y, Yoshikawa A, Sekiguchi H, Takada M, Furu M, Saito S, Kataoka M, Abe H. Yagi TJSr: Label-free photoacoustic imaging of human palmar vessels: a structural morphological analysis. 2018;8(1):1–8.
336. Agrawal S. Kuniyil Ajith Singh M, Johnstonbaugh K, C Han D, R Pameijer C. Kothapalli S-RJS: Photoacoustic imaging of human vasculature using LED versus laser illumination: A comparison study on tissue phantoms and in vivo humans. 2021;21(2):424.
337. Bar-Zion A, Yin M, Adam D. Foster FSJCR: Functional flow patterns and static blood pooling in tumors revealed by combined contrast-enhanced ultrasound and photoacoustic imaging. 2016;76(15):4320–31.
338. Xiao W, Li Y, Hu C, Huang Y, He Q, Gao H. Melanin-originated carbonaceous dots for triple negative breast cancer diagnosis by fluorescence and photoacoustic dual-mode imaging. J Colloid Interface Sci. 2017;497:226–32.
339. Shrestha B, Stojkova K, Yi R, Anastasio MA, Ye JY. Brey EMJAB: Gold nanorods enable noninvasive longitudinal monitoring of hydrogels in vivo with photoacoustic tomography. 2020;117:374–83.
340. Na S, Russin JJ, Lin L, Yuan X, Hu P, Jann KB, Yan L, Maslov K, Shi J, Wang DJJNBE: Massively parallel functional photoacoustic computed tomography of the human brain. 2021:1-9.
341. Na S. Wang LVJBOE: Photoacoustic computed tomography for functional human brain imaging. 2021;12(7):4056–83.
342. Prakash J, Kalva SK, Pramanik M. Yalavarthy PKJJoBO: Binary photoacoustic tomography for improved vasculature imaging. 2021;26(8): 086004.
343. Lin L, Hu P, Tong X, Na S, Cao R, Yuan X, Garrett DC, Shi J, Maslov K. Wang LVJNc: High-speed three-dimensional photoacoustic computed tomography for preclinical research and clinical translation. 2021;12(1):1–10.
344. Lutzweiler C, Razansky DJS. Optoacoustic imaging and tomography: reconstruction approaches and outstanding challenges in image performance and quantification. 2013;13(6):7345–84.
345. Yu Q, Liao Y, Liu K, He Z, Zhao Y, Li F, Shan T. Registration of photoacoustic tomography vascular images: Comparison and analysis of automatic registration approaches. Frontiers in Physics. 2022;10:1199.
346. Nico B, Benagiano V, Mangieri D, Maruotti N, Vacca A, Ribatti DJH. Evaluation of microvascular density in tumors, pro and contra. Histol Histopathol. 2008;23(5):601–7.
347. Hansen S, Grabau D, Sørensen FB, Bak M, Vach W. Rose CJBjoc: Vascular grading of angiogenesis: prognostic significance in breast cancer. 2000;82(2):339–47.
348. Tsuji-Tamura K, Morino-Koga S, Suzuki S, Ogawa M. The canonical smooth muscle cell marker TAGLN is present in endothelial cells and is involved in angiogenesis. J Cell Sci. 2021;134(15):jcs254920.
349. Morikawa S, Baluk P, Kaidoh T, Haskell A, Jain RK. McDonald DMJTAjop: Abnormalities in pericytes on blood vessels and endothelial sprouts in tumors. 2002;160(3):985–1000.

Publisher's Note